Remote Sensing of Environment 302 (2024) 113994

Contents lists available at ScienceDirect

Remote Sensing of Environment

journal homepage: www.elsevier.com/locate/rse

Long-term ice mass changes in Greenland and Antarctica derived from satellite laser ranging

Filip Gałdyn [a,*], Krzysztof Sośnica [a], Radosław Zajdel [a], Ulrich Meyer [b], Adrian Jäggi [b]

[a] Wrocław University of Environmental and Life Sciences, Institute of Geodesy and Geoinformatics, Grunwaldzka Str. 53, 50-357 Wrocław, Poland
[b] University of Bern, Astronomical Institute, Sidlerstrasse 5, 3012 Bern, Switzerland

ARTICLE INFO

Editor Name: Dr. Menghua Wang

Keywords:
Ice mass balance
Time-variable gravity field determination
GRACE
GRACE follow-on
SLR
Earth's gravity models

ABSTRACT

Time-variable gravity field models obtained from satellite gravimetric techniques allow for the assessment of ice sheet mass changes in remote polar regions, such as Greenland and Antarctica. So far, GRACE has been the primary mission for obtaining the global time-variable gravity field models. However, GRACE was launched in 2002, thus very little is known about the global mass changes before this data, as well as between GRACE and its successor – GRACE Follow-On. We derive a method of gravity field recovery based on Satellite Laser Ranging (SLR) data to geodetic satellites that allows for obtaining direct ice mass change estimates for a period longer by 10 years than that provided by the GRACE missions. The developed method is based on splitting normal equation systems and re-stacking the solutions which allow for stable inversion, reduces the correlations between obtained parameters, stabilizes the ice mass estimates in polar regions, and reduces the noise over oceans by a factor of four. The secular trends obtained from SLR are equal to −113.5 and −82.8 Gt/year, whereas these are −119.1 and −83.3 Gt/year from GRACE and GRACE-FO to degree and order 10 for Greenland and West Antarctica, respectively, for the common period of 2002–2021 and after removing the post-glacial rebound effect. Despite the conformity of the trend and patterns, an underestimation is observed in the solutions expanded to degree and order 10. Therefore, scaling factors between GRACE/GRACE-FO expanded up to a degree and order 10 × 10 and 60 × 60 were derived and applied to SLR solutions to account for the differences in mass estimates due to the truncation of the models. SLR data revealed that in Greenland the smallest ice mass trends are for 1995–2000, 2000–2005, and 2015–2020 which are equal to +54.3, −15.5, and −75.9 Gt/year. The largest ice mass depletion periods took place in 2005–2010, 2010–2015, and recently in 2019–2021 with trends of −213.9, −287.2, and −276.1 Gt/year, respectively. For Greenland and West Antarctica, the period 2010–2015 is characterized by the most enormous ice depletion events, whereas the later 5-year period of 2015–2020 provided a near mass-equilibrium for Antarctica reducing the negative trend and returning to the situation from the '90s when no significant ice mass changes were observed.

1. Introduction

The Earth's time-variable gravity field provides information on the redistribution of mass within the Earth system, including the ice sheet mass change. Previous research has shown that in some areas the ice mass is decreasing compared to previous levels (Rodell et al., 2018). This is particularly noticeable in places where ice sheets or glaciers are melting due to the effects of climate change (Luthcke et al., 2013; Velicogna et al., 2014). As a consequence of ice mass changes in high mountain glaciers, freshwater resources are modified, which may have a significant impact on natural ecosystems and human life. The long-term observations of the ice mass loss in Greenland and Antarctica are of special interest to justify whether the trends observed in recent years are in fact semi-constant or the ice mass depletion started to accelerate during the previous decade due to climate change. Greenland and Antarctica constitute very hard-to-reach regions for direct measurement, therefore, satellite remote sensing methods are best suited for assessing the changes in such regions (Tepes et al., 2021; Wang et al., 2023). However, the quality of satellite remote sensing data in the previous century and the limited long-lasting satellite missions strongly restricted the possibility of long-term ice mass change recovery in the polar regions (Syed et al., 2010).

* Corresponding author.
E-mail address: filip.galdyn@upwr.edu.pl (F. Gałdyn).

https://doi.org/10.1016/j.rse.2024.113994
Received 25 October 2023; Received in revised form 29 December 2023; Accepted 7 January 2024
Available online 15 January 2024
0034-4257/© 2024 The Authors. Published by Elsevier Inc. This is an open access article under the CC BY-NC license (http://creativecommons.org/licenses/by-nc/4.0/).

The understanding of mass transport within the Earth system was significantly improved after the launch of the Gravity Recovery and Climate Experiment (GRACE) mission in 2002 (Tapley et al., 2004). Using GRACE data, we can obtain time series of mass change over Greenland and Antarctica (Jacob et al., 2012; Shepherd et al., 2012, 2020; Velicogna and Wahr, 2013). Although the GRACE-based global models provide valuable information on the time-variable gravity field, the noise reduction using smoothing filters and regularization is necessary to extract the information from the measured observables. After 2010, GRACE data is affected by missing K-band observables during eclipsing seasons, whereas the last months of missions carry a negative impact caused by switching off the accelerometer to preserve battery cells. Another limitation is that data of the same spatial resolution is not available before the mission's launch date. Earth mass change data are currently being acquired by its successor, GRACE Follow-On, which was launched in 2018 one year after the end of the first GRACE mission (Landerer et al., 2020). In addition to dedicated missions, we can also acquire time-variable gravity field using different techniques, such as observations from satellite laser ranging (SLR) (Löcher and Kusche, 2021; Meyer et al., 2019; Sośnica et al., 2015), GPS-based orbit of low-orbiting satellites such as the Swarm mission (Dahle et al., 2020), data combinations of hydrological models and various missions (Richter et al., 2021), or observations from Global Navigation Satellite Systems (GNSS) using inverted methods (Blewitt, 2003; Wu et al., 2006).

Considering the paucity of GRACE data, the one-year gap existing between the GRACE and GRACE Follow-On missions, and that the data are available from April 2002, alternative techniques are sought to describe changes in gravitational potential on a global scale. Over the years, there have been publications attempting to use the SLR technique to retrieve the time-variable gravity field and, consequently, changes in the Total Water Storage (TWS). The SLR-based gravity field models have been determined with low resolution expanded in terms of spherical harmonics up to degree and order 4 (Matsuo et al., 2013), 5 (Cheng, 2017), 6 and 10 (Sośnica et al., 2015), the latter with additional constraints. These models can both be used to determine changes in TWS a decade before the GRACE period, but also during gaps between GRACE and GRACE Follow-On missions and during periods of malfunctioning GRACE missions. SLR observations to geodetic satellites began in the '70s with the launch of Starlette and LAGEOS-1 (Pearlman et al., 2019a) satellites, however, the quality and quantity of data before the '90s do not allow deriving global gravity field models with sufficient spatial resolution. Moreover, the SLR-based models have shown that it is challenging to determine changes for small areas, such as single river basins, because of limited model resolution. The solutions are very often uncertain and the changes cover a much larger area than the occurrence of the ice mass depletion.

The observations to laser geodetic satellites (Pearlman et al., 2019a) have also been used to determine the Earth's low-degree static gravity field (Maier et al., 2012), or to determine zonal spherical harmonic variations (Bianco et al., 1998; Cheng et al., 1997). Typically, the analysis has been limited to degree 2 coefficients, which are well recoverable from SLR data (Bloßfeld et al., 2015; Chen and Wilson, 2003, 2008; Chen et al., 2009). SLR observations to geodetic satellites provide the best estimates of the Earth's oblateness term (degree-2), Earth's center-of-mass position (degree-1), and the Earth's standard gravitational product GM (degree-0) (Pearlman et al., 2019a). Moreover, in the letter part of the GRACE mission and during the entire GRACE Follow-On mission the degree-3 C_{30} values are being replaced by SLR-based estimates because of the existence of nongeophyscical signals in the GRACE-based coefficients caused by the accelerometer failures (Cheng and Ries, 2023; Loomis et al., 2020; Loomis et al., 2019; Sun et al., 2023).

In this research, we determine the long-term time-variable Earth's gravity fields derived using a combination of SLR data. The variations of the global gravity field are determined for 27 years in the period 1995–2021 using low-degree Stokes coefficients to degree and order 10 based on SLR data only. So far, the SLR-based gravity field models had low spatial resolution because of the large noise for coefficients higher than degree 6. To obtain stable results from the SLR data with improved spatial resolution, we test several solutions expanded up to degree and order 4, 6, 8, and 10 and stack the normal equation systems taking a benefit from the stability of low-degree spherical harmonics and a better resolution of high-degree solution expansion. In this way, no constraints on gravity field coefficients are needed, which typically leads to the underestimation of the gravity signal (Meyer et al., 2019). The global gravity field models are used to derive the ice mass depletion trends in Greenland, as well as in the West and East Antarctic. Due to the fact that SLR models recover the total gravity field changes, the impact of the solid Earth changes due to post-glacial isostatic adjustment (GIA) must be subtracted to obtain the ice mass changes. The SLR-derived long-term ice mass changes for Greenland and Antarctica are compared with external gravity field models based on GRACE/GRACE-FO data, as well as other ice sheet mass balance models.

2. Data and methods

The Earth's gravitational potential can be represented as a series of spherical harmonic coefficients:

$$V(r,\phi,\lambda) = \frac{GM_E}{R}\sum_{n=0}^{\infty}\left(\frac{R}{r}\right)^{n+1}\sum_{m=0}^{n}P_{nm}(sin\phi)(C_{nm}cosm\lambda + S_{nm}sinm\lambda) \quad (1)$$

where r, ϕ, λ are the spherical coordinates in the reference frame, GM_E is the product of the gravitational constant and the Earth's mass, R is the semi-major axis of the Earth, C_{nm} and S_{nm} are the Stokes coefficients of spherical harmonics of degree n and order m, and P_{nm} are the fully normalized Legendre polynomials. After removing the solid Earth variations effects, such as solid Earth tides and pole tides, most of the gravity field changes observed are caused by fluid layers in the Earth's surface shell. Thus, the most commonly used representation for the gravity field comparison is the Equivalent Water Height (EWH), which represents the temporal (e.g. monthly) variations within the Earth's water cycle. By determining this parameter for each longitude and latitude, we can study its spatial distribution. Comparisons are then made in areas characterized by their intense variations in EWH parameter. From the individual spherical harmonic values, the EWH parameter is calculated as:

$$EWH_{(\phi\lambda)} = \frac{M_E}{4\pi R^2}\sum_{n=2}^{\infty}\frac{2n+1}{1+k_n}\sum_{m=0}^{n}P_{nm}(sin\phi)(\Delta C_{nm}cosm\lambda + \Delta S_{nm}sinm\lambda) \quad (2)$$

where k_n are the elastic load Love numbers of degree n, M_E is the Earth's mass, and ΔC_{nm} and ΔS_{nm} are temporal variations of the Stokes coefficients. The Δ indicates that the values are after subtracting the signal of the static gravity field part. In this study we used static coefficient of GOCO06s (Kvas et al., 2021) for this purpose. To compare the available models from different sources and techniques, the spherical harmonics coefficients are derived using consistent models following the International Earth Rotation Service and Reference Systems (IERS) Conventions 2010 (Petit and Luzum, 2010) with Atmosphere and Ocean Dealiasing Models RL06 (AOD, Dobslaw et al., 2017).

We determine the Earth's gravity field coefficients from SLR observations based on two high-orbiting LAGEOS satellites and up to seven low-orbiting satellites: Starlette, Stella, AJISAI, LARES, Larets, BLITS, and Beacon-C (Pearlman et al., 2019a) (Table 1). The perturbations of continuous dynamic orbits, i.e., the deviations from Keplerian orbits, are used to recover the Earth's gravity field which is for low-Earth-orbiters, the major cause of observed orbit perturbations. We derive the SLR-only gravity field solutions with the expansion up to degree and order 10/10 following the methodology described in Sośnica et al. (2015) using the developed version of the Bernese GNSS Software (Dach et al., 2015). The

Table 1
Orbit characteristics of geodetic satellites used for time-variable gravity field recovery.

Satellite	Launch date	Orbit altitude	Inclination	Mass	A priori error
Beacon-C	1965	940–1300 km	41.23°	32 kg	50 mm
Starlette	1975	800–1100 km	49.84°	47 kg	20 mm
LAGEOS-1	1976	5860 km	109.90°	407 kg	8 mm
AJISAI	1986	1500 km	50.04°	685 kg	25 mm
LAGEOS-2	1992	5620 km	52.67°	405 kg	8 mm
Stella	1993	810 km	98.57°	48 kg	20 mm
Larets	2003	690 km	97.77°	23 kg	30 mm
LARES	2012	1440 km	69.56°	387 kg	15 mm

standard procedure of SLR-based gravity field recovery (named **SLR F**) consists of three steps. First, we generate 1-day normal equations individually for each low-orbiting satellite, and 10-day normal equations for LAGEOS-1/2. Then, 10-day solutions are obtained by combining SLR observations for all satellites by stacking all common parameters from the normal equations, except for the orbital parameters, which are pre-eliminated before stacking so that they are only implicitly included in the resulting normal equation. The commonly estimated parameters contain SLR station coordinates, Earth rotation parameters, geocenter coordinates, and gravity field parameters (Sośnica et al., 2015). In the final step, monthly solutions are generated by stacking all parameters from the three 10-day normal equations and by imposing minimum rotation and translation constraints on the core stations in the network (Zajdel et al., 2019). We generate the solutions with a temporal resolution of one month from January 1995 to October 2021.

We derive global time-variable gravity field models using different approaches of normal equation handling. The first solution is based on the normal equations expanded to degree and order 10 (**SLR F**, following Sośnica et al. (2015)). The solution based on the least-squares adjustment can be written as follows:

$$\boldsymbol{x}_{10,10}^{SLR\ F} = \left(\boldsymbol{N}_{10,10}\right)^{-1} \boldsymbol{b}_{10,10}, \tag{3}$$

where $\boldsymbol{x}$ corresponds to the vector of unknown spherical harmonic coefficients C_{nm} and S_{nm}, $\boldsymbol{N}_{10,10}$ is the normal equation matrix based on the $\boldsymbol{A}$-design matrix and stochastic model $\boldsymbol{P}$, i.e., $\boldsymbol{N}_{10,10} = \boldsymbol{A}^T\boldsymbol{P}\boldsymbol{A}$ with all previously pre-eliminated parameters other than spherical harmonics, and $\boldsymbol{b}_{10,10}$ corresponds to the right-hand side of the normal equation system as a function of the true observation corrections $\boldsymbol{l}$, i.e., $\boldsymbol{b}_{10,10} = \boldsymbol{A}^T\boldsymbol{P}\boldsymbol{l}$ also including implicitly information about all pre-eliminated parameters, such as SLR station coordinates, Earth rotation parameters, range biases, and satellite orbits. The instability of the **SLR F** solution is caused by sparse SLR observations and large correlations between spherical harmonic coefficients that cause similar orbit perturbations for geodetic satellites. Sośnica et al. (2015) proposed introducing constraints on coefficients between degrees 6 and 10 or expanding the solution up to degree and order 6/6 to avoid instabilities of higher-degree coefficients. However, both approaches resulted in signal damping leading to the underestimation of the gravity signal when compared to GRACE-based solutions.

To stabilize the solution, we determine the gravity field models for a given month based on the coefficients of three months using the **SLR F** solution with the previous, the next and the month for which the gravity field coefficients are determined in the **SLR R** solution. However, this approach results in multiple uses of the same data and is similar to the low-pass filter of obtained coefficients.

In order to keep the monthly resolution of the models, we developed another method of stabilizing normal equation systems. The normal equation systems can be split into solutions expanded to a reduced degree by deleting unwanted parameters. From the normal equations expanded up to degree and order 10, i.e., $\boldsymbol{N}_{10,10}$, one can obtain the gravity field solutions expanded to, e.g., degree and order 4, i.e., $\boldsymbol{N}_{4,4}$ whose inversion is much more stable than that of $\boldsymbol{N}_{10,10}$ due to the reduced number of estimated parameters and thus reduced correlations.

The **SLR N** solution is obtained by stacking the previously split normal equations:

$$\boldsymbol{x}_{10,10}^{SLR\ N} = \left(\boldsymbol{N}_{10,10} + \boldsymbol{N}_{8,8} + \boldsymbol{N}_{6,6} + \boldsymbol{N}_{4,4}\right)^{-1} \left(\boldsymbol{b}_{10,10} + \boldsymbol{b}_{8,8} + \boldsymbol{b}_{6,6} + \boldsymbol{b}_{4,4}\right). \tag{4}$$

Note that the "+" sign denotes the process of stacking normal equations and not the simple sum as the $\boldsymbol{N}_{n,n}$ matrices and $\boldsymbol{b}_{n,n}$ vectors have different dimensions. The proposed solution takes full advantage of the expansion into degree 10 and the same spatial resolution as in $\boldsymbol{N}_{10,10}$, as well as the stabilities of low-degree gravity field solutions, e.g., $\boldsymbol{N}_{4,4}$, which provides superior coefficient estimates. The numerical inversion of the sum of normal equations $\boldsymbol{N}_{10,10} + \boldsymbol{N}_{8,8} + \boldsymbol{N}_{6,6} + \boldsymbol{N}_{4,4}$ is much more stable than the single $\boldsymbol{N}_{10,10}$ because the values of off-diagonal elements are reduced compared to the diagonal terms. Moreover, the proposed solution requires no constraints to a priori or external models, thus, the estimated gravity field coefficients can be derived as free parameters as opposed to the solution proposed by Sośnica et al. (2015). Please note that Eq. 4 is equivalent to re-scaling or re-weighing specific parts of the normal equation systems, therefore, the proposed method can be considered a variation of the weighting approach with increasing the contribution of the low-degree terms. However, weighting in this approach is applied to specific parts of the normal equations and not to the observations or the whole normal equation systems as typically considered in the least-squares theory.

SLR S solution is based on **SLR N**, however, three consecutive monthly solutions are stacked to reduce the noise of estimated parameters, especially in months with sparse SLR observations.

Then, we apply the weights by increasing them according to an increasing degree and order. This solution is called **SLR Q** with weights w_i increasing linearly to the maximum expansion of the gravity field model ($w_{10} = \frac{10}{4} = 2.5$, $w_8 = \frac{8}{4} = 2.0$, $w_6 = \frac{6}{4} = 1.5$, $w_4 = \frac{4}{4} = 1$):

$$\boldsymbol{x}_{10,10}^{SLR\ Q} = \left(w_{10}\cdot\boldsymbol{N}_{10,10} + w_8\cdot\boldsymbol{N}_{8,8} + w_6\cdot\boldsymbol{N}_{6,6} + w_4\cdot\boldsymbol{N}_{4,4}\right)^{-1} \left(w_{10}\cdot\boldsymbol{b}_{10,10} + w_8\cdot\boldsymbol{b}_{8,8} + w_6\cdot\boldsymbol{b}_{6,6} + w_4\cdot\boldsymbol{b}_{4,4}\right). \tag{5}$$

In **SLR Q,** the largest weights are thus given to normal equations that provide non-redundant information, whereas the smallest weight is given to the normal equations with the largest redundancy. The inverted normal equation system corresponds to covariance matrix $\boldsymbol{C}$ multiplied by the square of the unit weight ${m_o}^2$, i.e., $\boldsymbol{C} = {m_o}^2\boldsymbol{N}^{-1}$. Therefore, we propose another weighting scheme, but this time with weights increasing as the square of the maximum degree of the expansion:

$$\boldsymbol{x}_{10,10}^{SLR\ T} = \left({w_{10}}^2\cdot\boldsymbol{N}_{10,10} + {w_8}^2\cdot\boldsymbol{N}_{8,8} + {w_6}^2\cdot\boldsymbol{N}_{6,6} + {w_4}^2\cdot\boldsymbol{N}_{4,4}\right)^{-1} \left({w_{10}}^2\cdot\boldsymbol{b}_{10,10} + {w_8}^2\cdot\boldsymbol{b}_{8,8} + {w_6}^2\cdot\boldsymbol{b}_{6,6} + {w_4}^2\cdot\boldsymbol{b}_{4,4}\right). \tag{6}$$

In the next solution, **SLR P**, we impose constraints on the gravity field coefficients from degree 7 to degree 10 of $2.5x10^{-10}$, which is similar to the solution proposed by Sośnica et al. (2015), but may result in the time-variable gravity signal damping because constraints are introduced with respect to the a priori static gravity field model. In **SLR W,** constraints are imposed on zonal harmonics only due to the largest correlations between zonal terms of the same parity. This solution can be sought as an alternative to deriving so-called lumped gravity field

Table 2
Description of developed and analyzed SLR solutions.

Solution	Description
SLR F	raw, unconstrained, SLR-only, 1-month solutions
SLR R	3-month solutions based on three consecutive SLR F normal equations
SLR N	1-month solutions based on SLR F normal equations split into the maximum expansion to degree and order 4, 6, 8, 10, and re-stacked again with equal weights
SLR S	3-month solution based on three consecutive SLR N solutions
SLR Q	similar to SLR N but with weights linearly increased for high-degree normal equations
SLR T	similar to SLR N but with weights increased for high-degree normal equations as squares of the maximum degree expansion
SLR W	SLR F solutions with constraints introduced on zonal harmonics
SLR P	SLR F solutions with constraints introduced on harmonics of degrees from 7 to 10

parameters. All remaining gravity field coefficients – sectorial and tesseral – are estimated as unconstrained parameters in **SLR W**.

Table 2 summarizes all the solutions giving a short description of the approach used to derive the solution.

We compare SLR-based solutions with other techniques or combinations of techniques for gravity field recovery and ice mass balance estimations. We use GRACE and GRACE Follow-On data based on operationally combined monthly gravity fields (Meyer et al., 2020a; Meyer et al., 2020b). We also use a long time-series of the hybrid SLR-GRACE approach based on empirical orthogonal functions for recovering temporal gravity field models (Löcher and Kusche, 2021), as well as the GRACE-based ITSG-Grace2018 model derived by Mayer-Gürr et al. (2018). We also compare our solutions with monthly gravity field models based on high-low satellite-to-satellite tracking (HLSST) (Weigelt, 2019) and from the Ice sheet mass balance inter-comparison inter-technique combination (IMBIE; Otosaka et al., 2023).

3. Time-variable gravity field derived from satellite techniques – method validation

We derive the long-term time-variable gravity field models based on SLR and we convert the results to EWH and estimate ice mass change (Eq. 2). We validate our models by the comparison with GRACE and GRACE Follow-On and other techniques by looking at the correlation coefficients in derived trends, correlations of individual spherical harmonics, as well as Root Mean Square (RMS) errors over selected areas. We have identified four typical regions with high variability in EWH to investigate the possibility of mass redistribution recovery and the correlation between models determined with SLR data and GRACE and GRACE Follow-On data. These are the areas of Greenland, West Antarctica, and Scandinavia, which show a strong trend, but also an area with strong seasonal changes - the Amazon.

3.1. Validation of SLR-based gravity field models – gravity signal

The monthly changes in EWH determined from the SLR-based models are compared to GRACE and GRACE Follow-On models based on operationally combined monthly gravity fields from the International Combination Service for Time-variable Gravity Fields (COST-G) which is a product center of the International Gravity Field Service (IGFS) of the International Association of Geodesy (IAG, Meyer et al., 2020a; Meyer et al., 2020b). Moreover, we compare SLR solutions to other publicly available models, such as hybrid temporal gravity fields based on empirical orthogonal functions (IGG SLR Hybrid) (Löcher and Kusche, 2021), ITSG-Grace2018 (Mayer-Gürr et al., 2018), and monthly gravity field models based on HLSST, i.e., kinematic orbits of low orbiters based on GPS data (Weigelt, 2019). Each of the models was expanded up to a degree and order 10/10 for comparison purposes, thus, GRACE and HLSST models do not require any spatial filters which are needed for the model expansions up to higher degrees.

Fig. 1 shows changes in terms of the mass anomaly in Greenland between January 1995 and October 2021 in Giga tons of EWH and shows differences between selected SLR solutions. The periods before the launch of GRACE and between GRACE and GRACE Follow-On are marked in violet, whereas the gaps in GRACE data due to eclipsing periods and battery issues are marked in grey. The SLR solutions are fully continuous over the whole analyzed period, however, with increased noise in the ‘90s. This comparison shows that the signals from the SLR technique and GRACE/GRACE-FO in the Greenland region are approximately equal when expanded to degree and order 10.

SLR F solution is characterized by the largest noise in Fig. 1, which is due to the instability of the normal equation inversion with a gravity field model expansion up to degree and order of 10 without any constrains. Splitting normal equation systems with re-stacking substantially reduces the noise which results in secular mass trends similar to that from GRACE for the **SLR N**, **SLR Q**, and **SLR S** solutions. **SLR S** is further smoothed, especially in the ‘90s because three consecutive normal equation systems were stacked, resulting in 3-month solutions.

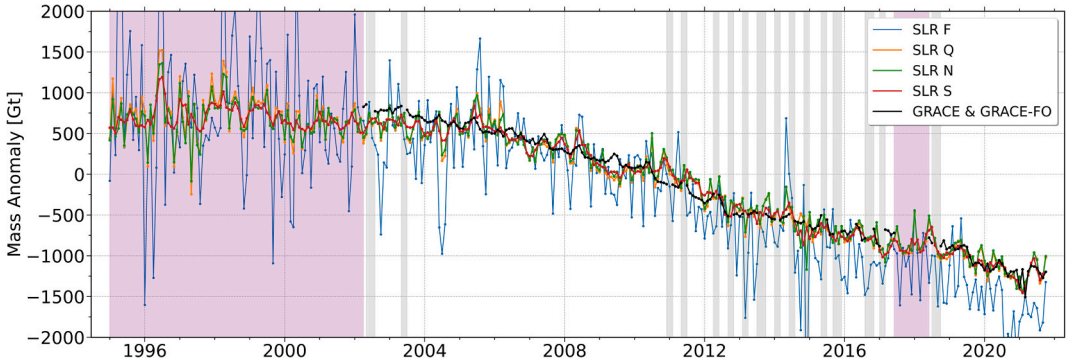

Fig. 1. Long-term mass variations over Greenland derived from selected SLR models and GRACE and GRACE-FO COST-G solutions, with coefficients truncated up to degree and order 10. The mass anomaly is given in Giga tons. The grey vertical areas indicate the absence of GRACE data due to battery issues and the purple areas indicate the absence of a mission dedicated to measuring the gravity field – prior to the GRACE launch or the gap between GRACE and GRACE Follow-On. (For interpretation of the references to colour in this figure legend, the reader is referred to the web version of this article.)

Interestingly, the models obtained from the SLR data do not indicate any significant mass loss in the Greenland area for the period before the launch of GRACE or during the gap between GRACE and GRACE Follow-On observations. We can also see a slight inconsistency between the SLR and GRACE data for the initial period of GRACE, i.e. 2002.4–2004. The GRACE data indicate that the process of the ice mass depletion started soon after the mission launched, whereas the SLR data show that the acceleration started around 2005. This effect has also been noted by Bonin et al. (2018) and Meyer et al. (2019). It is noteworthy that there is a very high agreement between the SLR data and the data from the GRACE Follow-On gravity field satellite mission, except for the **SLR F** which shows a distinct offset with respect to other solutions. This means that SLR models based on split normal equations can be used to retrieve continuous long-term gravity field changes, whereas raw solutions, denoted as **SLR F,** are very unstable. However, we have to decide which approach performs best: **SLR N**, **SLR Q**, **SLR S** or the others.

Fig. 2 shows the Pearson correlation between the mass anomaly changes in the Greenland area from the different models. We analyze the maximum lengths of periods that are available for each model. To extend the series length for GRACE and GRACE Follow-On, we combine them into a single series. Each of the analyzed solutions has a strong positive correlation with values starting at around 0.7. The highest correlation with the GRACE COST-G solution is found for the models based also on GRACE data (ITSG), employing GRACE for the extraction of the empirical orthogonal function coefficients (IGG SLR Hybrid) or models using strong noise reduction filters and GPS data onboard low satellites, including GRACE (HLSST). Compared to the latter, the SLR solutions are the only ones that are fully independent of GRACE data and can entirely be derived in the absence of the GRACE mission. **SLR S**, **SLR N**, and **SLR Q** solutions have the highest correlations out of the models we have identified that are based solely on laser observations to geodetic satellites. For the SLR S solution, this value is about 0.98 relative to GRACE and GRACE Follow-On, HLSST and ITSG models. The unconstrained, raw, **SLR F** solution has the lowest and most divergent correlation with the GRACE solutions. Interestingly, **SLR S** has larger correlation coefficients with GRACE and HLSST models than with other SLR solutions, such as **SLR R**, **SLR Q** and **SLR P**, despite that **SLR S** is based on exactly the same observations with only different handling of normal equation regularization. **SLR R**, which is a 3-month version of **SLR F**, is characterized by inferior performance when compared to other SLR and GRACE solutions. Similarly, the **SLR P** solutions with constraints imposed on coefficients between degrees 7 and 10 are inferior due to the damping of some gravity field signals by aligning the gravity field variations to the a priori models. **SLR W** with stabilization of the zonal terms only by introducing parameter constraints performs better than **SLR P** and **SLR F**, however, worse than **SLR N** and **SLR Q**.

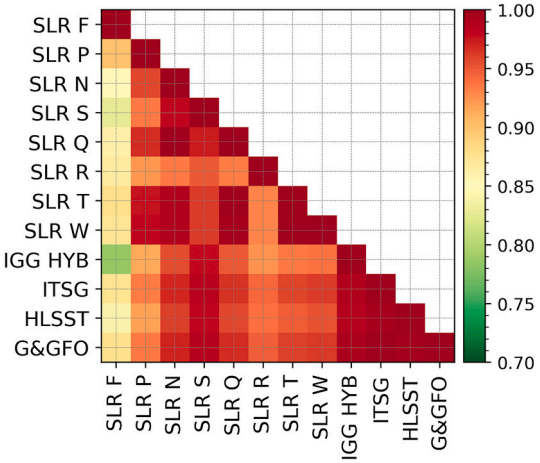

Fig. 2. EWH correlation coefficient between SLR models, GRACE models, and HLSST for the gravity signals in the Greenland region. All solutions are truncated to degree and order 10.

Fig. 3 illustrates the secular changes of the Earth's gravity field in terms of EWH for the period 2002.4–2021.10 to compare SLR-based models with GRACE and GRACE Follow-On solutions. Each of the solutions, as in Fig. 3, is expanded up to a degree and order of 10. We can see that even with limited spatial resolutions, it is possible to detect trends in global gravity change, especially in high-latitude areas affected by ice mass loss. Comparing the SLR solutions, we see that splitting the normal equations in the **SLR N** and **SLR S** strategies leads to a reduction in noise in ocean areas where no secular gravity changes are expected and a reduction in trends in dryland areas. Despite the limited spatial resolution of SLR solutions, the trends due to GIA in Scandinavia and North America are fully recoverable. However, in **SLR F** the GIA signal has a similar magnitude to the noise, whereas, in **SLR S** and **SLR N**, the GIA signal can be distinguished from the solution artifacts. The negative trends in the Caspian Sea area are consistent between **SLR S/N** and GRACE solutions as shown in Fig. 3. The effect of both negative and positive trends can be seen in the Antarctic region which are caused mainly by GIA and ice sheet mass depletion, respectively. The gravity field signal can be retrieved for Antarctica despite the lack of SLR stations and thus the lack of SLR observations of geodetic satellites collected in the South Pole region (Sośnica et al., 2015). The dynamic orbits of geodetic satellites carry information about the total gravity field of the Earth included in the secular and periodical changes of the Keplerian orbit parameters irrespectively where the direct laser ranging observations are collected.

The correlations for the Amazon region, West Antarctica, and Scandinavia are shown in Fig. 4. These results confirm the correlations determined for the Greenland area and show that in these areas the **SLR N**, **SLR S**, and **SLR Q** models have the highest values of the correlation parameter with respect to the solutions derived from the GRACE data. These solutions, even in areas as small as Scandinavia, show correlations in the range of 0.6–0.8, in contrast to the **SLR F** solution, where values relative to the GRACE solution in these areas are between 0.2 and 0.5. Therefore, the method of splitting normal equations employed in SLR N-like solutions is superior when compared to other techniques of SLR solutions including the constraining of high-degree coefficients, constraining zonal coefficients, or deriving inversions of raw solutions from **SLR F**.

3.2. *Validation of SLR-based gravity field models – spherical harmonics*

The correlation analysis illustrated in Fig. 2 and Fig. 4 and the comparison in Fig. 1 show a high consistency between the GRACE and GRACE Follow-On observations and the 3-month **SLR S** model and 1-month **SLR N** model. Despite using the same observations in all SLR normal equations, different results are obtained depending on the explicit constraints on parameters or implicit constraints based on splitting normal equations. Therefore, we decided to look at the correlations within the individual spherical harmonics of the split model from SLR N and compare them with the original **SLR F** solution without normal equation modifications to find the source of the stabilization of the obtained gravity signals.

Fig. 5 shows a comparison of the absolute values of correlation coefficients derived from covariance matrices $\boldsymbol{Cov} = m_o^2 N^{-1}$ between the spherical harmonics in the **SLR F** (in grey) and the **SLR N** solutions (in green). The correlation coefficient between the i and the j spherical harmonics reads as:

$$\mathrm{Corr}_{ij} = \frac{Cov_{xx,ij}}{\sqrt{Cov_{xx,ii} \cdot Cov_{xx,jj}}} \tag{7}$$

where $\mathrm{Cov}_{xx,ii}$ and $\mathrm{Cov}_{xx,jj}$ are the diagonal elements of the $\boldsymbol{Cov}$ matrix describing the variances of the i and the j spherical harmonic, and $\mathrm{Cov}_{xx,ij}$ is the off-diagonal element (covariance) between the i and the j

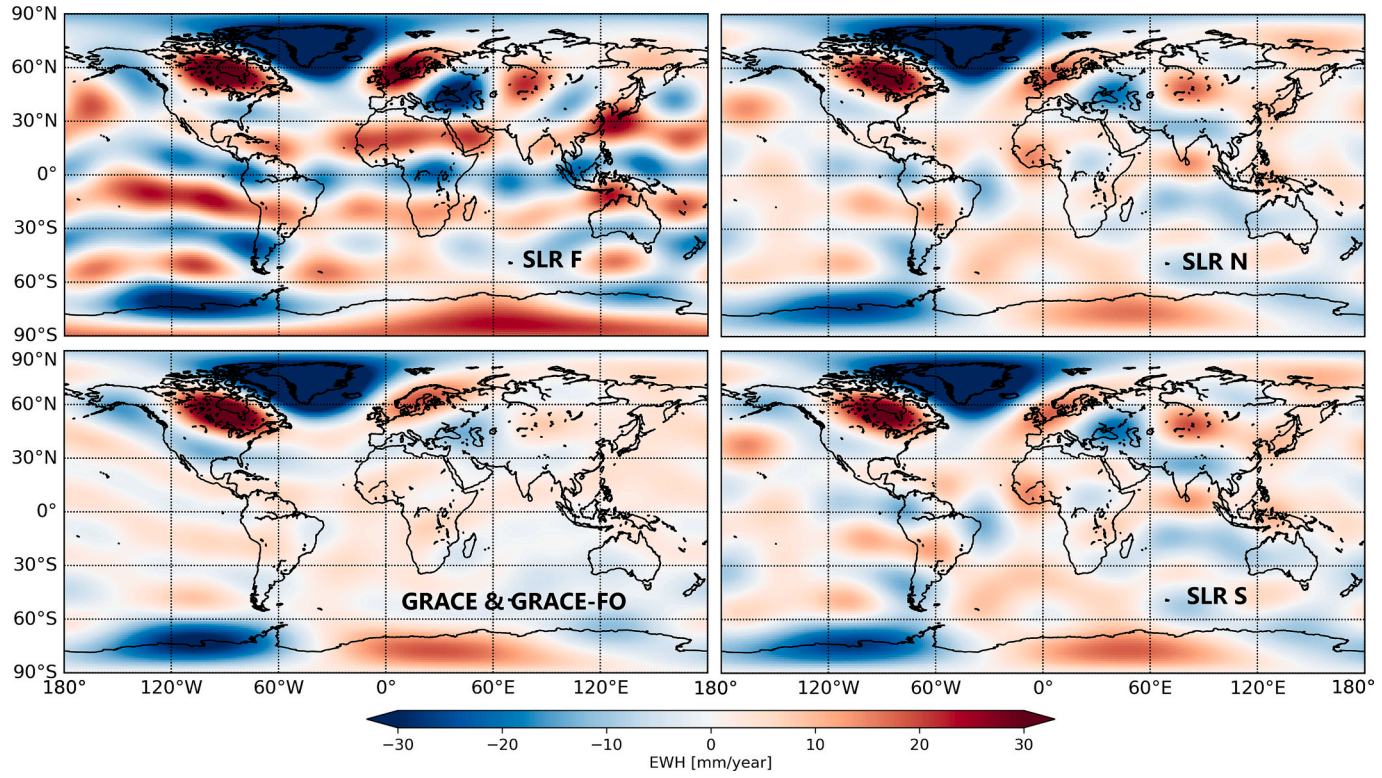

Fig. 3. Global secular trends of EWH, upper left – SLR F, upper right – SLR N, bottom left – GRACE and GRACE Follow-On, bottom right – SLR S. The solutions cover the period 2002.4–2021.10. All solutions are truncated to degree and order 10.

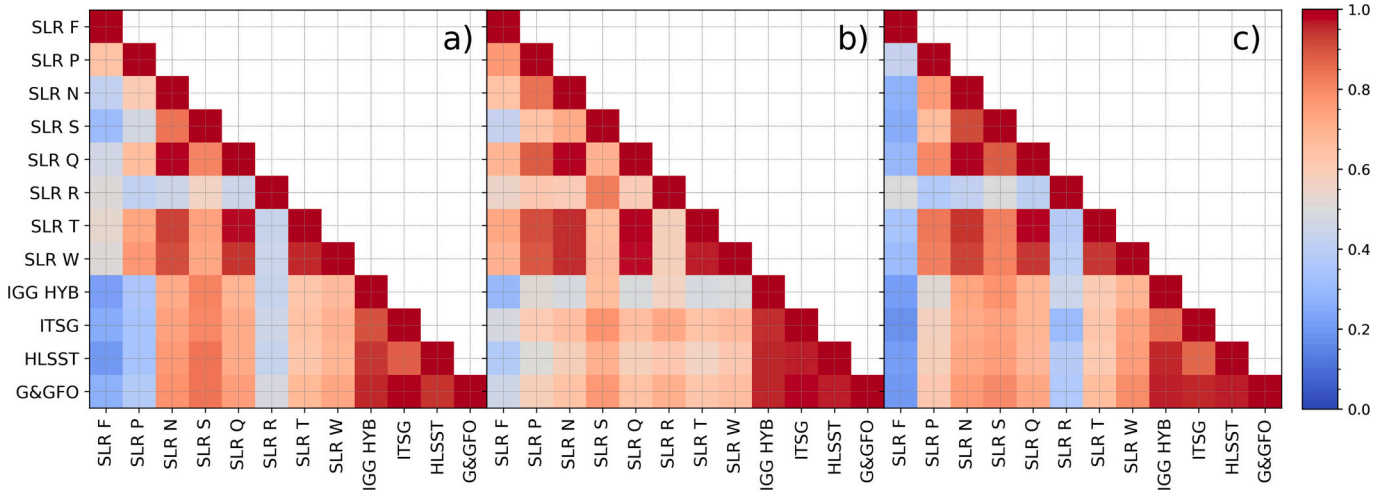

Fig. 4. EWH correlation coefficient for the gravity field signal in the a) Amazon, b) Scandinavia, and c) West Antarctica regions. All solutions are truncated to degree and order 10.

spherical harmonic. We have extracted only those correlations that had values greater than or equal to 0.8 in the **SLR F** solution. The values were sorted in descending order of the difference in the correlations between **SLR F** and **SLR N**. The right-hand side of Fig. 5 shows the percentages of the number of spherical harmonics that have the largest correlations in **SLR F** and **SLR N** presented in the form of bars with different intervals represented by different colors. Most of the largest correlations are obtained for zonal harmonics of the same parity, e.g., $C_{2,0} \sim C_{4,0} \sim C_{6,0} \sim C_{8,0} \sim C_{10,0}$ or coefficients of the same order and the degree of the same parity, e.g., $S_{5,5} \sim S_{7,5}$, $S_{2,1} \sim S_{6,1}$, $C_{8,6} \sim C_{10,6}$.

Fig. 5 shows how the correlations of each spherical harmonic have been changed due to the process of splitting and re-stacking normal equations. At the highest threshold – for correlations above 0.6, only the correlation between $C_{2,0}$ and $C_{4,0}$ remains in **SLR N**, whereas in **SLR F** correlations for many coefficients still exceed 0.8. For instance, the correlations between zonal harmonics $C_{5,0} \sim C_{9,0}$, $C_{6,0} \sim C_{10,0}$, $C_{4,0} \sim C_{10,0}$, $C_{2,0} \sim C_{10,0}$ are reduced from the level of 0.95 to 0.05, thus, completely de-correlated. In total, 97% of the correlations are in the lowest correlation range – below 0.2 for the **SLR N** solution. For the **SLR F** solution, the number of coefficients with correlations below 0.2 equals around 92%. Therefore, the stabilization of the solution is mostly obtained by a substantial reduction of the correlation between estimated parameters despite that **SLR F** and **SLR N** are based on exactly the same observations. Further spherical harmonics validation analyses can be

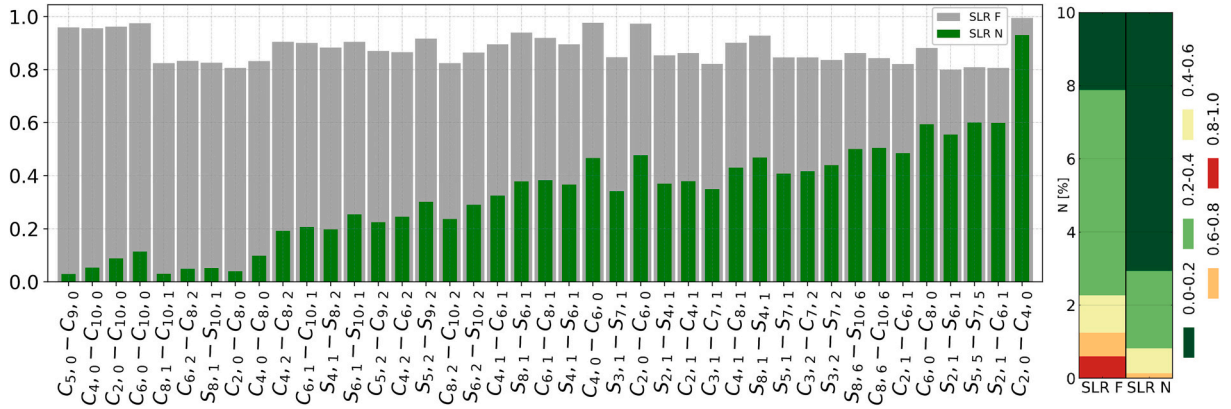

Fig. 5. Comparison of the absolute correlation between estimated spherical harmonics for the SLR F and SLR N solutions (left). Only spherical harmonic pairs with a correlation coefficient above a value of 0.8 in the SLR F model are shown in descending order of the difference between the level of correlation reduction between SLR F and SLR N. The right figure shows the percentage of spherical harmonic pairs belonging to each interval of the correlation level. The area highlighted in dark green is the complement up to 90%. (For interpretation of the references to colour in this figure legend, the reader is referred to the web version of this article.)

found in Appendix B and C.

3.3. Validation of SLR-based gravity field models – Noise over oceans

In the next step, we validate the gravity field model using the median RMS residuals of the EWH in an inner part of the Pacific Ocean. We use an area of about 92 million square kilometers. As shown by Chen et al. (2021), the mean RMS over the open ocean is much smaller than over land after removing the linear trend and annual and semi-annual variability. The land areas are dominated by large intra-seasonal EWH signals which are not present over oceans. In the ocean areas, one of the major changes may be seafloor deformation and large-size earthquakes. However, earthquakes and seafloor deformations induce small systematic signals, and thus, the variability in the oceans shall be qualified as a noise, which gives an indication of the quality of the model determined.

The results shown in Fig. 6 and Table 3 validate the SLR models, HLSST, and SLR hybrid IGG models against the GRACE and GRACE Follow-On solutions. Again, large noise with RMS of EWH in the Pacific equal to 34 cm is observed for **SLR F**. The noise is reduced by a factor of four in **SLR S** w.r.t. **SLR F**. The median noise of the GRACE solutions, which is 3.2 cm, is a factor of two smaller than the best **SLR S** solution (7.7 cm). HLSST, despite employing strong Kalman filtering, is characterized by RMS at a comparable level to **SLR S**. Hence, the normal equation splitting in SLR solutions remarkably reduces the noise of gravity signals over oceans.

The individual peaks seen in Fig. 6 in the **SLR F** solution reach up to 120 cm and indicate its instability. The **SLR N** solutions also show a peak

Table 3
Median RMS of EWH in the inner part of the Pacific Ocean for SLR and GRACE solutions expanded to degree and order 10 cover the period 2002.4 through 2021.10.

Solution	Median RMS [cm]
SLR F	33.9
SLR N	9.7
SLR S	7.7
SLR Q	10.7
IGG HYB	3.0
HLSST	6.4
GRACE + GFO	3.2

at the beginning of 2004, 2006, and 2015, which can be related to the number of available SLR observations during the winter season December/February with large overcast skies in the northern hemisphere and thus lack of laser observations. The upward trend of the errors in each of the solutions since the beginning of 2011 is also noteworthy, which can be caused by the a priori reference frame – ITRF2014. The a priori reference frame includes observations only up to the end of 2014, therefore, the solutions in the later epochs are based on extrapolations which do not consider discontinuities caused by equipment changes, earthquakes or non-linear station motions included in post-seismic deformation coefficients. In the early periods of data, **SLR S** solutions are superior when compared to HLSST, whereas, after 2016, HLSST becomes better than the SLR-based solutions, most possibly

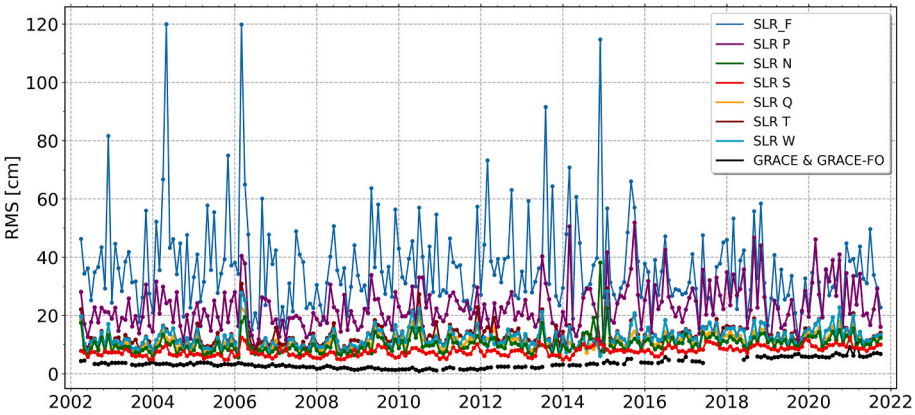

Fig. 6. Monthly time series of average RMS residuals in EWH from different SLR solutions and GRACE and GRACE Follow-On COST-G. Solutions cover the period 2002.4 through 2021.10 over the part of open ocean.

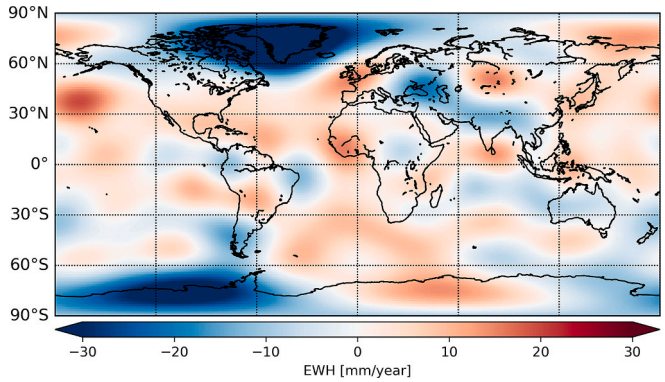

Fig. 7. The secular trend in EWH from the SLR N after correcting for the GIA effect. The solution covers the period 2002.4 through 2020.12.

because of the increasing number of low Earth orbit (LEO) satellites equipped with GPS receivers and high-quality accelerometers onboard (Mao et al., 2021).

Out of all analyzed SLR solutions, **SLR N** and **SLR S** provide the best results in the majority of validation indicators. Therefore, for the final assessments of the ice sheet mass trends, only these two solutions will be considered as those that are characterized by superior performance.

Further evaluation of the SLR-based solutions are provided in Appendix B and C which include a study of formal errors of the estimated parameters and a comparison of spherical harmonics with GRACE data, respectively.

4. Results on the ice sheet mass depletion estimates

As the next step, the ice mass changes from GRACE and SLR are compared to those determined using a combination of techniques and sources as provided by the Ice-sheet Mass Balance Inter-comparison Exercise (IMBIE) for Greenland and Antarctica[1] (Otosaka et al., 2023; Shepherd et al., 2018, 2020). A comparison with the independent model is indispensable to verify the derived SLR models and the accuracy of the determination of ice mass changes in the Greenland and Antarctic regions. Moreover, IMBIE data are available also for the '90s prior to the GRACE launch. IMBIE also includes data obtained by radar and laser altimetry, as well as data obtained by calculating the difference between precipitation and runoff, sublimation and ice loss as well as GRACE data.

4.1. Long-term gravity field changes and the comparison with IMBIE data

Now, we perform the comparison in the Greenland region, for West and East Antarctica. To compare satellite gravimetric trends with the IMBIE data, the post-glacial isostasy must be reduced from satellite data, as it may have a significant impact on the obtained results (Wake et al., 2016), especially in Antarctica. We removed the GIA effect using the model proposed by (Caron et al., 2018). Fig. 7 highlights the EWH trends after the removal of the GIA effect. The data for Greenland are very consistent, as the GIA secular trends expanded up to degree 10 are not large in this region. However, most of the gravity field changes observed in North America and Scandinavia from SLR-based models are completely eliminated when reducing the GIA effects. Hence, SLR can also be employed for the recovery of large-scale long-term changes in solid Earth and not only in the outermost Earth fluid layers.

Table 4 shows the overall mean ice mass depletions for the common periods – starting from 2002 (beginning of GRACE series) to 2021 (end of IMBIE series). For Greenland, the mean trends from data expanded to degree and order 10 are consistent and equal to −108.8 and −110.7 Gt/year for **SLR S** and GRACE, respectively. Fig. 8 and Table 4 show that some inconsistencies between the ice mass depletion estimates occurred after 2004 between IMBIE and two space gravimetric techniques – SLR and GRACE derived from the solutions with the expansion up to degree and order 10. Interestingly, all models show a change in the trend around 2016–2018 with the swap in the slope to positive which corresponds to ice mass accumulation in this period. After 2018, GRACE and SLR show consistent negative slopes again. **SLR S** agrees well with IMBIE in the '90s when GRACE data are not available. The ice sheet mass in Greenland before 2002 was close to equilibrium with no significant changes. Despite the conformity of the patterns, an underestimation is observed in the data expanded to degree an order 10 for the Greenland region as shown in Fig. 8 and Table 4. Based on this information, we derive a scaling factor between GRACE/GRACE-FO expanded up to 10 × 10 and GRACE/GRACE-FO up to 60 × 60 to account for the differences in mass estimates due to the truncation of the models. The derived scaling factors based on the least-squares analysis are equal to 1.73, 1.59 and 0.54 for Greenland, West and East Antarctica, respectively. The GRACE-based scaling factors are then applied to the rescaling SLR 10 × 10 solutions to account for the limited SLR capabilities in the recovery of high-degree gravity field coefficients. The original SLR estimates and those after scaling are shown in Fig. 8. Solutions to degree and order 60 × 60 are also included for those models for which such solutions are available. GRACE solutions up to 60 × 60 also do not fully follow the IMBIE estimates, but it is worth noting that they have not been subjected to any averaging filters. Despite the underestimation of the total masses in the solution expanded up to degree and order 10, the overall patterns are consistent and reflect large-scale changes, whereas the rescaled SLR solutions correspond well with IMBIE, especially before the launch of GRACE.

Table 4
Comparison of trends over the period 2002.04 to the end of IMBIE series i.e., 2020.12. All solutions are after removing the GIA effect.

	2002.04–2020.12 [Gt/year]		
	GREENLAND	WEST ANTARCTICA	EAST ANTARCTICA
SLR N 10 × 10	−106.8	−92.1	10.1
SLR S 10 × 10	−108.8	−92.9	14.4
IMBIE	−237.8	−120.1	6.5
GRACE+GFO 10 × 10	−110.7	−105.0	9.0
GRACE+GFO 60 × 60	−194.0	−170.4	−9.5
SLR S sc	−188.9	−148.1	7.8
SLR N sc	−185.5	−146.8	5.5

Also of note in Fig. 8 are the areas associated with the Antarctic regions. In these areas, the trends determined by the SLR technique are broadly consistent with the IMBIE estimates. The Antarctic regions are larger than those in Greenland, therefore, the scaling factor is smaller. Increasing the resolution of the solution up to degree 60 does not lead to a change of the trend magnitude in Antarctica as prominently as in the case of Greenland.

For West Antarctica, the secular mass trends equal −92.9 and −105.0 Gt/year in **SLR S** and GRACE models 10 × 10, respectively. For West Antarctica, SLR solutions are quite noisy, especially before 2012 due to sparse SLR observations collected at high latitudes in the southern hemisphere. Nevertheless, the long-term trends agree well between SLR and GRACE in the solutions of the same expansion, i.e., 10 × 10. Some gravity signals could be lost due to omission errors related to the solution expansion and thus the limited spatial resolution and the leakage of some masses into neighbouring areas. For West Antarctica, GRACE solutions become also noisy after 2014 – in the last stage of the mission and after 2020 when GRACE Follow-On should provide stable solutions. Inner Antarctic structure, in terms of the gravity field change distribution, cannot be well recovered from SLR because none of the SLR

[1] http://imbie.org/data-downloads

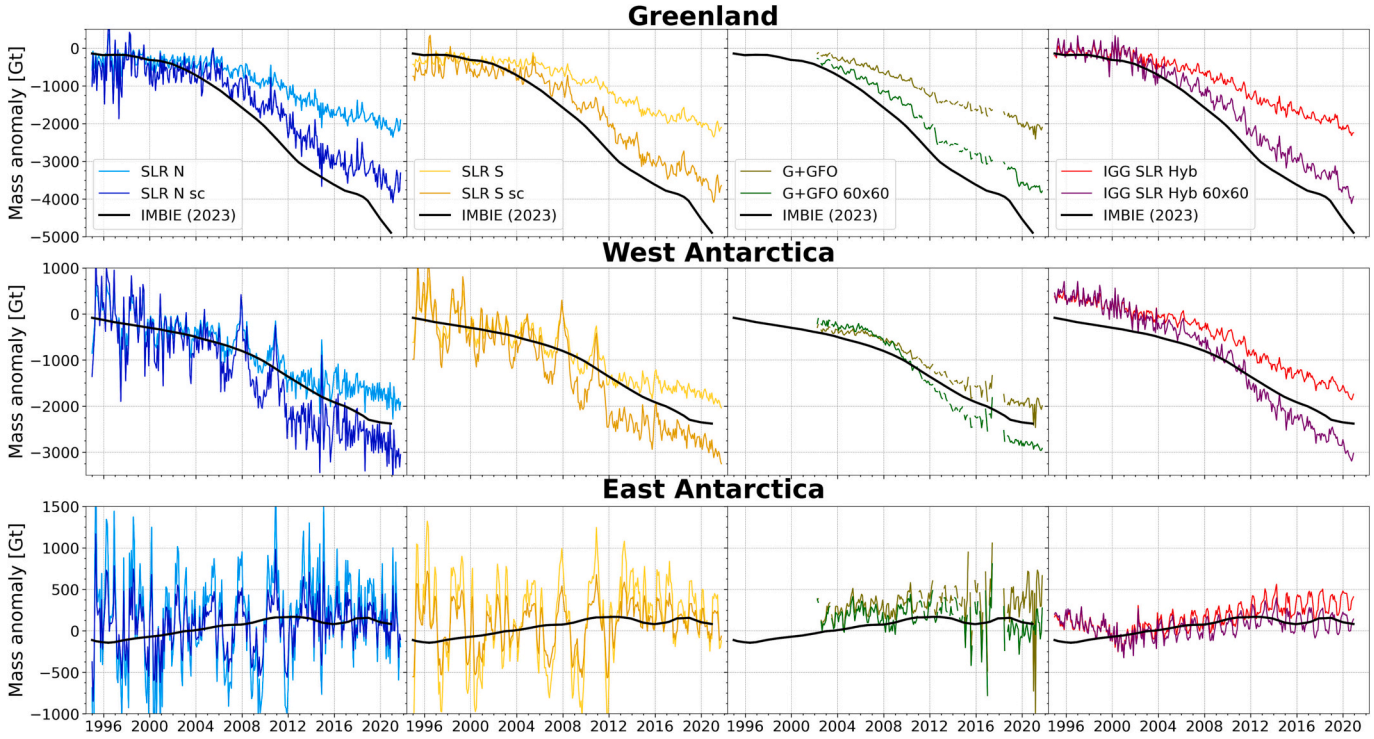

Fig. 8. The cumulative ice-sheet mass changes from SLR N, SLR S, GRACE and GRACE Follow-On, and IGG SLR Hybrid models for Greenland (top), West Antarctica (middle) and East Antarctica (bottom) to degree and order 10 and 60. IMBIE values are shown for comparison in black. The darker shade of colour indicates scaled values of solutions by considering a scaling factor (sc) calculated between GRACE and GRACE-FO data up to degrees and orders 10 and 60. All solutions are unfiltered solutions.

observations were directly collected over Antarctica due to the lack of stations in this region. Nevertheless, dynamic orbits of geodetic satellites inherently carry information about the mass distribution in the whole Earth system, which is why SLR allows for the recovery of large-scale gravity field changes in remote areas.

Satellite gravimetry data for East Antarctica are affected by the largest noise in both SLR and GRACE solutions. IMBIE provides a small ice mass increase of +6.5 Gt/year. However, for this region, disagreements may emerge from inferior quality of satellite gravimetry data as well as errors in the background GIA model, which is affected by the largest uncertainty in the areas permanently covered by ice sheets.

4.2. Time-variable gravity field changes for polar regions in 5-year windows

We derive the ice mass trends by fitting deterministic models in 5-year periods from SLR and GRACE data with applied scaling factor calculated in Section 4.1. We show these fitted values for the Greenland region in Fig. 9 and summarize the secular trends in Table 5.

In the first period 1995–1999, denoted P1, i.e., prior to the GRACE mission, there is no significant negative trend. The **SLR S** and **SLR N** solutions show a positive trend of +54.3 ± 21.6 and +65.1 ± 43.4 Gt/year, respectively, whereas the IGG SLR Hybrid model shows a negative trend of −38.4 ± 25.6 Gt/year. The IGG SLR Hybrid model extracts the

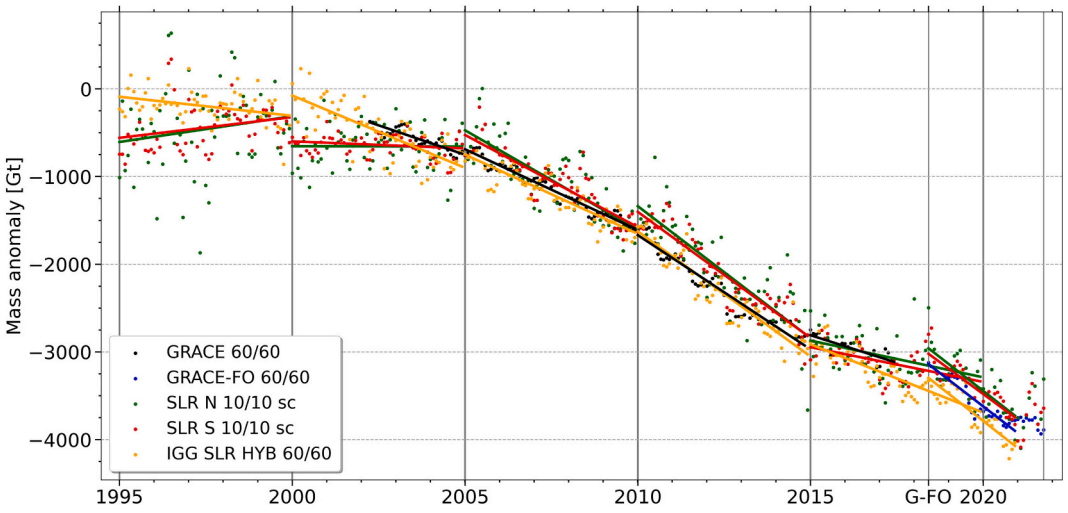

Fig. 9. Mass anomalies in Greenland from GRACE and SLR models and best fitting trends for 5-year periods and GRACE-FO period. The GIA effect is removed. The scaling factors for data derived to degree and order 10 are applied.

Table 5
Ice sheet mass trend estimates in Greenland from GRACE and SLR for 5-year periods in the Greenland region with correcting for the GIA model and with applied scaling factors.

Data period		Solution	Trend and error [Gt/year]
P1	1995.1–1999.12	SLR N sc	65.1 ± 43.4
		SLR S sc	54.3 ± 21.6
		IGG SLR HYB 60/60	−38.4 ± 14.6
		IMBIE	−25.6 ± 1.8
P2	2000.1–2004.12	SLR N sc	1.1 ± 22.4
		SLR S sc	−15.5 ± 11.1
		IGG SLR HYB 60/60	−158.0 ± 18.1
		IMBIE	−120.1 ± 3.4
	2002.4–2004.12	GRACE 60/60	−124.0 ± 8.2
P3	2005.1–2009.12	SLR N sc	−229.8 ± 22.5
		SLR S sc	−213.9 ± 14.6
		IGG SLR HYB 60/60	−172.4 ± 8.2
		GRACE 60/60	−179.3 ± 3.8
		IMBIE	−237.3 ± 1.0
P4	2010.1–2014.12	SLR N sc	−303.4 ± 26.1
		SLR S sc	−287.2 ± 15.8
		IGG SLR HYB 60/60	−279.6 ± 13.3
		GRACE 60/60	−254.5 ± 9.0
		IMBIE	−279.2 ± 4.2
P5	2015.1–2019.12	SLR N sc	−78.1 ± 20.6
		SLR S sc	−75.9 ± 13.3
		IGG SLR HYB 60/60	−148.8 ± 11.2
		IMBIE	−179.0 ± 6.2
	2015.1–2017.6	GRACE 60/60	−127.6 ± 19.2
P6	2018.6–2020.12	SLR N sc	−292.7 ± 45.2
		SLR S sc	−276.1 ± 21.9
		GRACE FO 60/60	−294.2 ± 21.7
		IGG SLR HYB sc	−300.4 ± 23.7
		IMBIE	−407.7 ± 3.9

main orthogonal function coefficients based on GRACE data which are always characterized by negative trends in Greenland. In IGG SLR Hybrid solutions, SLR is used for rescaling the trends in areas identified by GRACE to be affected by major changes. However, when different areas would be affected by mass changes prior to the GRACE mission, the IGG SLR Hybrid approach cannot identify and recover such changes. From the IMBIE data, the trend over the period P1 is −25.6 ± 1.8 Gt/year. Please note, however, that the IMBIE model in the '90s incorporates a limited number of techniques for the ice mass trends, therefore, the errors in the IMBIE models are larger in P1 and P2 than in the subsequent periods.

For the period 2000–2004, denoted P2, the trend values are −15.5 ± 11.1 and +1.1 ±22.4 Gt/year for **SLR S** and **SLR N**, respectively, −158.0 ± 18.1 Gt/year for IGG SLR Hybrid, and −120.1 ± 3.4 Gt/year for the IMBIE data. GRACE data are incomplete or of inferior quality in this period due to the initial mission phase.

There is a high consistency between all models for the periods 2005–2009 and 2010–2014, labelled P3 and P4, respectively. For these periods, a relative error of −3% and −11% for period P3 and 8% and 3% for period P4 is obtained for **SLR N** and **SLR S** models, respectively, w.r.t. to the IMBIE data. The trends derived from SLR S equal −229.8 ± 22.5 and −213.9 ± 14.6 Gt/year, whereas from IMBIE these are −237.3 ± 1.0 and −279.2 ± 4.2 Gt/year for P3 and P4, respectively. In contrast, these errors are −38% and −10% for the GRACE data w.r.t. IMBIE data.

For period P6, the trends are −292.7 ± 45.2, −276.1 ± 21.9, −300.4 ± 23.7, and 407.7 ± 3.9 Gt/year for **SLR N**, **SLR S**, GRACE-FO, and IMBIE respectively. Based on Fig. 1 and the marked breaks in the models, we can see that the periods with the fewest grey boxes indicating missing data have the highest agreement of the GRACE/GRACE Follow-On data with the determined SLR models. As explained by Meyer et al. (2019), the solutions expanded up to degree 10 are underestimated concerning GRACE solution up to degree 60 due to omission errors and data leakage. However, Meyer et al. (2019) used SLR gravity field models with constraints for degrees 7–10, which is similar to the **SLR P** solution from this study characterized by inferior performance w.r.t. **SLR N** and **SLR S** solutions. SLR solutions in this study are not constrained towards the a priori values and, in addition, are rescaled to the solutions expanded up to degree and order 60 to avoid signal dumping and omission errors. In Fig. 9, the trends of the ice mass depletion accelerated again in the last period P6, which is consistently observed in all the analyzed solutions. The ice mass losses after 2020 are again as large as in the periods 2005–2010 and 2010–2015, i.e., with the maximum depletion of the ice sheet as observed so far.

Fig. 10 shows the ice mass change estimates for Greenland and West Antarctica for all periods from SLR data derived up to degree and order 10 with applied scaling factors. Again, the largest negative trends are obtained for periods P3, P4, and P6, whereas periods P1, P2, and P5 are typically characterized by small trends in mass changes. The largest trend in West Antarctica equals −290.0 ± 33.6 Gt/year in P4, i.e., in 2010–2015; whereas the trend is about zero in P2 (2000–2005) and equals −0.3 ± 30.6 Gt/year from SLR S. The IGG SLR Hybrid model tends to overestimate the ice mass loss in the last period P6 for West Antarctica with trends of −234.0 ± 20.8 Gt/year, especially when compared to GRACE Follow-On which gives values of −66.5 ± 14.1 Gt/year. GRACE indicates even an opposite, positive trend in P5, which is a result of a considerable number of data gaps in GRACE observations, a gap between GRACE and GRACE Folow-On missions, as well as inferior quality of GRACE observations after the deactivation of some instruments, including the onboard accelerometer. Contrary to GRACE, SLR solutions have a similar quality over the last 20 years with a small improvement in 2013 when LARES was launched; therefore, SLR can be used to fill up the gap between GRACE and GRACE Folow-On, and in future, between GRACE Folow-On and its successor.

Fig. 10 suggests that the trends in West Antarctica derived from SLR solutions seem to have a larger dynamic than those derived from IMBIE.

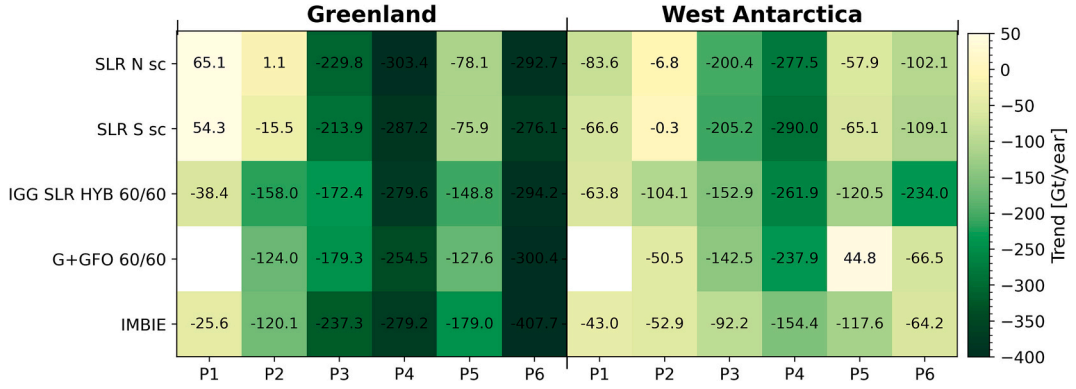

Fig. 10. The EWH trends derived from different models for Greenland and West Antarctica. The GRACE/GRACE-FO data are expanded to degree and order 60. SLR data are expanded to degree and order 10 and rescaled by factor. The periods are defined in Table 4. The GIA effect is removed.

In periods P3 and P4, the SLR-based trend is −205.2 and −290.0 Gt/year, i.e., almost a factor of two larger than that derived from IMBIE, i.e., −92.2 and 154.4 Gt/year. On the other hand, periods P2 and P5 characterized in SLR solutions by small trends of −6.8 and −57.9 Gt/year are larger by about 50 Gt/year in the IMBIE solutions. The ice mass depletion in the polar regions should thus be considered as a process with a large time variability.

As opposed to the GRACE data, SLR solutions have not been integrated into the IMBIE combination. Table A.1 in the Appendix contains cumulative ice-sheet mass changes with uncertainties from SLR S for Greenland, West Antarctica and East Antarctica after GIA corrections for each month starting from January 1995. SLR solutions may still be affected by some modeling errors which requires further efforts to mitigate them. Nevertheless, the SLR technique has tremendous potential in the recovery of large-scale mass changes in the Earth system and offers GRACE-independent satellite gravimetric solutions.

5. Discussion and conclusions

We developed a method of time-variable gravity field recovery expanded to the degree and order of 10 based on SLR data which can be used for the recovery of time-variable gravity field in polar regions. The method is based on splitting the normal equations and re-stacking them again, which results in a substantial reduction of correlations between estimated parameters of spherical harmonics and allows for the stable inversion of the normal equation systems. As a result, the correlations between zonal harmonics, e.g., $C_{5,0} \sim C_{9,0}$, and $C_{2,0} \sim C_{10,0}$ are substantially reduced from the level of 0.95 to 0.05. The same effect is obtained for other harmonics with degrees of the same parity and orders of the same values. The method provides a stable inversion of the normal equations, which allows for the reduction of the solution noise in mass estimates. The noise over the Pacific Ocean in terms of RMS is reduced from 33.9 cm in standard SLR solution (**SLR F**) to 9.7 cm in 1-month solutions with splitting normal equations (**SLR N**) and to 7.7 cm in 3-month solutions (**SLR S**). The gravity field coefficients derived from SLR data are characterized by a large level of consistency with GRACE data with mean correlation coefficients above 0.4 for all spherical harmonics up to degree 8. Such a level of consistency was obtained only for degree 2 when using the standard SLR solution in **SLR F**.

The SLR allows for the ice sheet mass estimates of the polar regions. The secular trends obtained for Greenland are equal to −108.8 and −110.6 Gt/year whereas for West Antarctica these are −92.9 and −105.0 Gt/year from SLR and GRACE expanded to degree and order 10, respectively for the common periods and after removing the GIA effect. However, the SLR series is longer than the GRACE by almost 10 years, because SLR provides estimates prior to the GRACE launch, during the gap between GRACE and GRACE Follow-On missions, as well as during the periods of eclipsing seasons of GRACE satellites with the lack of GRACE K-band observations. Therefore, the SLR is capable of the recovery of long-term ice mass changes and their evolution over time.

The SLR data up to degree and order 10 aligns with IMBIE regarding the relative equilibrium of Greenland's ice mass in the 1990s. However, it only explains approximately 46% of the trend values observed in IMBIE data and 56% of trend values observed in GRACE expanded to degree and order 60 after 2002. This indicates that the expansion up to degree and order 10 requires applying a scaling factor of 1.74 for Greenland, which needs to be taken into account when employing this technique for estimating ice mass changes. The scaling factor was derived based on GRACE 10 × 10 and 60 × 60 solutions for the common period. Nevertheless, the overall patterns and the trends agree well between SLR, IMBIE and GRACE 60 × 60 after applying the scaling factor.

SLR data revealed that in Greenland the smallest ice mass trends are for 1995–2000, 2000–2005, and 2015–2020 which are equal to +54.3, −15.5, and −75.9 Gt/year, respectively when correcting for the GIA effect. The largest ice mass depletion periods took place in 2005–2010, 2010–2015, and recently in 2019–2021 with trends of −213.9, −287.2, and −276.1 Gt/year, respectively from SLR S solution after correcting for GIA and with the applied scaling factor. Therefore, the ice mass balance in the polar region must be considered a time-variable process with periods of both, moderate mass increase and substantial depletions.

Similarly to Greenland, for West Antarctica, the smallest rates of ice mass depletion are obtained in periods 1995–2000, 2000–2005, and 2015–2019 equaling −66.6, −0.3, and −65.1 Gt/year, respectively from SLR S solutions with GIA corrections and with the applied scaling factor. The secular rates were largest in 2005–2010, 2010–2015, and 2019–2022 with values of −205.2, −290.0, and −109.1 Gt/year, respectively from SLR S. Therefore, for both polar regions, the periods 2010–2015 turned out to be characterized by most tremendous ice depletion events. The later 5-year period of 2015–2020 provided a near-equilibrium for Antarctica reducing the negative trend and returning to the situation from the '90s. However, the most recent data show again an increase in ice mass depletion. Ice mass estimates for East Antarctica are problematic due to the large noise of satellite gravimetric solutions as well as large uncertainties in the background solid Earth isostasy models that have to be subtracted from satellite gravimetry data to obtain reasonable ice mass estimates. Nevertheless, the SLR observations to geodetic satellites provide valuable information on temporal changes of large-scale mass changes for the remote and hardly-reachable polar regions.

Funding

This work was supported by the National Science Centre, Poland (NCN), Grant No. UMO-2021/42/E/ST10/00020. The APC is financed by Wrocław University of Environmental and Life Sciences (UPWr).

CRediT authorship contribution statement

Filip Gałdyn: Software, Visualization, Writing – original draft. **Krzysztof Sośnica:** Writing – review & editing, Funding acquisition. **Radosław Zajdel:** Writing – review & editing. **Ulrich Meyer:** Software, Writing – review & editing. **Adrian Jäggi:** Software, Writing – review & editing.

Declaration of competing interest

The authors declare the following financial interests/personal relationships which may be considered as potential competing interests:

Filip Gałdyn reports financial support was provided by National Science Centre Poland. Krzysztof Sośnica reports financial support was provided by National Science Centre Poland.

Data availability

The gravity field data will be published on the International Centre for Global Earth Models (ICGEM) website.

Acknowledgements

We would like to acknowledge the International Laser Ranging Service (ILRS) (Pearlman et al., 2019a, 2019b) for providing SLR data. The Authors thank Dr. Matthias Weigelt for proving the HLSST gravity field solutions.

Appendix A

Table A.1
The cumulative ice-sheet mass changes from SLR S model for Greenland, West Antarctica and East Antarctica after GIA corrections.

Date	GREENLAND		WEST ANTARCTICA		EAST ANTARCTICA	
	Ice dynamics anomaly (Gt)	Rate of ice dynamics anomaly uncertainty (Gt/yr)	Ice dynamics anomaly (Gt)	Rate of ice dynamics anomaly uncertainty (Gt/yr)	Ice dynamics anomaly (Gt)	Rate of ice dynamics anomaly uncertainty (Gt/yr)
1995–01	0.0	74.0	0.0	170.8	0.0	103.7
1995–02	0.5	70.5	−4.7	162.8	−1.7	98.9
1995–03	−113.0	68.3	310.7	157.7	286.9	95.8
1995–04	226.3	67.1	843.2	155.1	799.1	94.2
1995–05	170.1	67.2	1146.7	155.3	1121.2	94.3
1995–06	119.6	68.1	2143.3	157.4	1115.2	95.6
1995–07	167.1	69.3	1815.1	160.1	836.9	97.2
1995–08	366.4	70.2	1107.5	162.1	704.4	98.4
1995–09	185.9	70.2	1099.0	162.0	674.3	98.4
1995–10	46.2	69.0	1032.2	159.4	625.8	96.8
1995–11	32.7	66.8	1375.2	154.2	621.5	93.7
1995–12	55.7	63.9	1665.3	147.7	858.1	89.7
1996–01	16.3	61.0	1624.3	140.9	755.4	85.5
1996–02	173.3	58.6	808.0	135.3	981.2	82.2
1996–03	80.1	57.2	1316.3	132.1	1157.3	80.2
1996–04	243.1	56.6	1489.5	130.7	1271.0	79.4
1996–05	585.2	56.7	2229.7	131.0	1234.1	79.5
1996–06	1039.1	57.3	1930.8	132.4	921.8	80.4
1996–07	1086.1	58.0	1631.4	134.0	619.1	81.4
1996–08	735.2	58.5	1191.5	135.2	577.1	82.1
1996–09	111.2	58.5	1004.8	135.2	618.5	82.1
1996–10	37.4	57.8	809.6	133.5	641.4	81.1
1996–11	−2.8	56.5	1142.6	130.6	802.7	79.3
1996–12	126.0	55.1	1296.5	127.2	969.7	77.3
1997–01	624.6	53.9	1202.7	124.4	919.2	75.6
1997–02	483.8	53.2	546.7	122.9	637.6	74.6
1997–03	503.2	53.1	517.2	122.6	384.8	74.4
1997–04	85.4	53.2	447.3	122.9	137.1	74.6
1997–05	306.2	53.3	379.1	123.2	216.1	74.8
1997–06	156.4	53.5	−116.2	123.5	26.1	75.0
1997–07	−6.7	53.5	−182.6	123.6	21.6	75.0
1997–08	−57.9	53.5	175.9	123.6	180.5	75.1
1997–09	4.7	53.5	562.4	123.6	456.8	75.0
1997–10	335.5	53.4	540.7	123.4	474.7	75.0
1997–11	491.2	53.5	474.3	123.7	474.6	75.1
1997–12	547.9	54.0	250.6	124.7	381.1	75.7
1998–01	521.9	55.0	129.7	126.9	418.0	77.1
1998–02	458.8	56.3	215.0	129.9	288.4	78.9
1998–03	496.7	57.4	333.0	132.6	434.1	80.5
1998–04	790.6	58.2	962.2	134.5	659.5	81.7
1998–05	452.3	58.4	1288.8	134.9	963.2	81.9
1998–06	406.1	58.0	1520.3	134.0	912.7	81.4
1998–07	389.1	57.4	1513.4	132.6	968.8	80.5
1998–08	558.8	56.9	1223.8	131.4	948.4	79.8
1998–09	434.9	56.9	993.2	131.3	920.4	79.7
1998–10	208.8	57.5	1054.8	132.8	805.0	80.6
1998–11	40.4	58.9	1022.8	136.1	695.9	82.6
1998–12	228.6	61.1	1258.8	141.0	855.9	85.6
1999–01	388.4	63.8	582.5	147.4	816.5	89.5
1999–02	402.8	66.6	565.1	153.8	844.4	93.4
1999–03	508.6	68.6	1120.9	158.5	977.1	96.2
1999–04	503.9	69.9	1153.6	161.4	1041.0	98.0
1999–05	438.5	70.1	1789.1	161.8	1003.0	98.3
1999–06	533.5	69.3	1597.9	160.2	823.4	97.3
1999–07	350.5	68.3	1208.1	157.7	681.7	95.8
1999–08	247.2	67.4	651.1	155.7	416.5	94.5
1999–09	78.0	67.4	353.9	155.6	174.2	94.5
1999–10	279.9	68.4	496.0	158.1	142.5	96.0
1999–11	378.7	70.8	556.1	163.5	175.0	99.3
1999–12	132.4	74.0	279.0	170.9	288.2	103.8
2000–01	193.2	37.9	480.4	104.8	472.0	69.9
2000–02	125.8	36.2	886.0	99.8	826.9	66.6
2000–03	120.6	35.0	704.1	96.7	962.6	64.5
2000–04	−12.4	34.4	791.5	95.1	537.9	63.4
2000–05	188.4	34.5	165.5	95.2	69.7	63.5
2000–06	41.4	35.0	29.9	96.5	23.3	64.4
2000–07	7.2	35.6	−169.9	98.2	47.8	65.5
2000–08	−35.0	36.0	113.4	99.4	231.7	66.3
2000–09	49.5	36.0	−49.9	99.4	248.0	66.3
2000–10	14.8	35.4	233.5	97.8	419.5	65.2

(*continued on next page*)

Table A.1 (*continued*)

Date	GREENLAND		WEST ANTARCTICA		EAST ANTARCTICA	
	Ice dynamics anomaly (Gt)	Rate of ice dynamics anomaly uncertainty (Gt/yr)	Ice dynamics anomaly (Gt)	Rate of ice dynamics anomaly uncertainty (Gt/yr)	Ice dynamics anomaly (Gt)	Rate of ice dynamics anomaly uncertainty (Gt/yr)
2000–11	138.7	34.2	719.2	94.6	240.2	63.1
2000–12	191.0	32.8	1109.0	90.6	214.8	60.4
2001–01	373.7	31.3	1068.2	86.4	174.7	57.6
2001–02	186.5	30.1	205.8	83.0	399.3	55.4
2001–03	179.7	29.4	132.0	81.1	322.3	54.1
2001–04	100.9	29.0	361.2	80.2	504.1	53.5
2001–05	265.8	29.1	623.5	80.3	488.3	53.6
2001–06	164.7	29.4	950.3	81.1	790.5	54.1
2001–07	131.6	29.8	577.7	82.2	739.0	54.8
2001–08	2.6	30.0	499.2	82.9	740.8	55.3
2001–09	34.1	30.0	452.4	82.9	658.2	55.3
2001–10	95.7	29.7	441.0	81.9	718.7	54.6
2001–11	155.5	29.0	450.1	80.1	557.3	53.4
2001–12	364.7	28.3	859.8	78.0	564.2	52.1
2002–01	186.2	27.6	382.9	76.3	439.0	50.9
2002–02	131.6	27.3	304.0	75.4	491.1	50.3
2002–03	−62.1	27.2	549.2	75.2	661.5	50.2
2002–04	−65.6	27.3	771.1	75.4	814.4	50.3
2002–05	52.3	27.4	1029.8	75.6	989.7	50.4
2002–06	171.9	27.4	961.0	75.7	936.4	50.5
2002–07	240.1	27.4	680.1	75.8	850.5	50.5
2002–08	248.1	27.5	625.1	75.8	695.0	50.6
2002–09	137.1	27.4	481.1	75.8	492.2	50.5
2002–10	141.6	27.4	313.6	75.7	304.9	50.5
2002–11	16.9	27.5	316.6	75.8	319.2	50.6
2002–12	221.2	27.7	313.2	76.5	400.9	51.0
2003–01	224.8	28.2	498.8	77.9	777.6	51.9
2003–02	218.9	28.9	926.0	79.7	974.3	53.2
2003–03	188.9	29.5	764.9	81.3	950.4	54.3
2003–04	105.3	29.9	691.2	82.5	753.7	55.0
2003–05	330.2	30.0	215.7	82.7	549.1	55.2
2003–06	155.5	29.7	−48.1	82.1	353.5	54.8
2003–07	74.1	29.4	−119.8	81.3	454.4	54.2
2003–08	58.6	29.2	−201.8	80.6	486.0	53.7
2003–09	69.8	29.2	−175.6	80.5	495.8	53.7
2003–10	193.8	29.5	40.6	81.4	628.2	54.3
2003–11	200.8	30.2	−35.9	83.4	612.6	55.7
2003–12	25.3	31.3	377.0	86.5	588.3	57.7
2004–01	−112.6	32.7	407.5	90.4	562.6	60.3
2004–02	−43.0	34.2	139.6	94.3	352.1	62.9
2004–03	−103.7	35.2	277.4	97.3	423.1	64.9
2004–04	68.4	35.9	312.2	99.1	578.9	66.1
2004–05	238.8	35.9	351.1	99.2	554.3	66.2
2004–06	−10.0	35.5	689.2	98.2	606.2	65.5
2004–07	−212.1	35.0	423.0	96.6	602.6	64.5
2004–08	−205.7	34.6	597.4	95.4	748.9	63.7
2004–09	−55.0	34.5	774.9	95.4	784.5	63.6
2004–10	168.7	35.1	781.5	96.9	792.3	64.7
2004–11	259.8	36.3	823.6	100.2	739.5	66.9
2004–12	113.3	38.0	981.9	104.8	885.2	69.9
2005–01	−11.2	49.8	703.6	160.0	779.8	85.2
2005–02	−15.1	47.4	491.4	152.5	715.9	81.1
2005–03	29.6	46.0	405.2	147.7	796.6	78.6
2005–04	42.9	45.2	460.7	145.3	789.3	77.3
2005–05	186.3	45.3	644.4	145.5	866.1	77.4
2005–06	537.3	45.9	666.6	147.5	856.2	78.5
2005–07	283.2	46.7	300.8	150.0	881.4	79.8
2005–08	342.7	47.3	242.9	151.9	879.2	80.9
2005–09	83.0	47.3	134.1	151.9	720.6	80.8
2005–10	90.7	46.5	−30.4	149.5	458.0	79.5
2005–11	72.3	45.0	11.9	144.6	347.8	76.9
2005–12	44.6	43.1	25.9	138.4	275.5	73.7
2006–01	−5.8	41.1	493.1	132.0	576.7	70.2
2006–02	−15.8	39.4	515.8	126.8	775.5	67.5
2006–03	75.1	38.5	240.2	123.8	833.3	65.9
2006–04	−24.9	38.1	31.0	122.4	696.8	65.2
2006–05	−71.0	38.2	−105.1	122.7	506.5	65.3
2006–06	−190.8	38.6	−392.6	124.0	309.3	66.0
2006–07	−187.4	39.1	−283.6	125.6	312.5	66.8
2006–08	−178.3	39.4	−434.8	126.7	258.2	67.5
2006–09	−141.7	39.4	−330.1	126.7	262.0	67.4
2006–10	−140.6	39.0	−522.7	125.2	156.3	66.6
2006–11	−109.6	38.1	−422.5	122.4	113.6	65.1

(*continued on next page*)

Table A.1 (*continued*)

Date	GREENLAND		WEST ANTARCTICA		EAST ANTARCTICA	
	Ice dynamics anomaly (Gt)	Rate of ice dynamics anomaly uncertainty (Gt/yr)	Ice dynamics anomaly (Gt)	Rate of ice dynamics anomaly uncertainty (Gt/yr)	Ice dynamics anomaly (Gt)	Rate of ice dynamics anomaly uncertainty (Gt/yr)
2006–12	−462.1	37.1	−265.6	119.2	171.8	63.5
2007–01	−527.9	36.3	−263.2	116.6	237.7	62.1
2007–02	−524.3	35.8	−546.4	115.2	294.3	61.3
2007–03	−395.6	35.7	−325.5	114.9	363.7	61.1
2007–04	−280.9	35.8	−323.5	115.1	366.6	61.3
2007–05	−160.2	35.9	−119.9	115.5	413.9	61.4
2007–06	−212.9	36.0	160.5	115.7	679.2	61.6
2007–07	−215.2	36.0	136.8	115.8	740.2	61.6
2007–08	−352.1	36.1	398.1	115.9	775.7	61.7
2007–09	−353.3	36.0	707.4	115.8	903.6	61.6
2007–10	−286.6	36.0	785.9	115.7	990.7	61.6
2007–11	−218.4	36.1	1031.0	115.9	1014.5	61.7
2007–12	−136.2	36.4	1279.0	116.9	1092.4	62.2
2008–01	−264.5	37.0	1040.0	119.0	994.6	63.3
2008–02	−378.0	37.9	849.6	121.8	885.7	64.8
2008–03	−559.8	38.7	653.0	124.3	782.8	66.2
2008–04	−417.3	39.2	509.4	126.1	785.4	67.1
2008–05	−162.4	39.3	489.3	126.4	652.4	67.3
2008–06	24.1	39.1	404.6	125.5	632.2	66.8
2008–07	−273.5	38.6	192.4	124.2	682.2	66.1
2008–08	−286.0	38.3	−185.5	123.1	678.0	65.5
2008–09	−458.6	38.3	−425.5	123.0	503.1	65.5
2008–10	−496.7	38.7	−607.3	124.4	278.7	66.2
2008–11	−702.5	39.7	−669.4	127.5	111.6	67.9
2008–12	−667.1	41.1	−755.4	132.2	138.3	70.4
2009–01	−703.6	43.0	−547.5	138.1	283.4	73.5
2009–02	−747.3	44.9	−476.5	144.2	382.1	76.7
2009–03	−760.8	46.2	−481.4	148.6	391.8	79.1
2009–04	−894.4	47.1	−381.5	151.3	457.5	80.5
2009–05	−848.4	47.2	−931.5	151.7	219.4	80.7
2009–06	−846.0	46.7	−947.7	150.1	124.0	79.9
2009–07	−870.9	46.0	−1101.1	147.7	52.8	78.6
2009–08	−975.3	45.4	−901.0	145.8	93.4	77.6
2009–09	−866.8	45.4	−1058.3	145.7	−7.5	77.6
2009–10	−704.8	46.1	−1089.4	148.1	132.9	78.8
2009–11	−678.6	47.7	−1039.8	153.2	254.8	81.5
2009–12	−803.6	49.8	−642.8	160.2	515.5	85.3
2010–01	−883.3	54.1	−694.8	115.0	597.1	79.2
2010–02	−841.3	51.5	−931.5	109.5	583.8	75.5
2010–03	−852.5	49.9	−657.6	106.1	712.0	73.1
2010–04	−772.7	49.1	−660.7	104.4	873.1	71.9
2010–05	−752.1	49.2	−504.7	104.5	878.8	72.0
2010–06	−678.0	49.8	−449.9	105.9	862.8	73.0
2010–07	−832.8	50.7	−460.9	107.7	868.5	74.3
2010–08	−835.7	51.3	−252.2	109.1	909.8	75.2
2010–09	−825.4	51.3	−109.9	109.1	894.2	75.2
2010–10	−757.9	50.5	174.4	107.3	964.4	74.0
2010–11	−560.8	48.8	454.4	103.8	1053.5	71.5
2010–12	−591.1	46.8	564.1	99.4	1230.2	68.5
2011–01	−739.2	44.6	145.7	94.8	1078.2	65.3
2011–02	−920.8	42.8	−230.9	91.1	984.3	62.8
2011–03	−968.1	41.8	−582.4	88.9	829.7	61.3
2011–04	−1164.4	41.4	−552.9	88.0	712.5	60.6
2011–05	−1037.7	41.5	−621.4	88.2	615.1	60.7
2011–06	−1028.5	41.9	−584.0	89.1	555.9	61.4
2011–07	−798.5	42.4	−468.4	90.2	755.2	62.2
2011–08	−973.2	42.8	−577.7	91.0	586.9	62.7
2011–09	−1006.2	42.8	−836.7	91.0	427.7	62.7
2011–10	−1082.6	42.3	−1079.8	89.9	172.6	62.0
2011–11	−1071.7	41.3	−1470.1	87.9	−15.2	60.6
2011–12	−1312.3	40.3	−1479.1	85.6	−5.5	59.0
2012–01	−1340.9	39.4	−1420.4	83.8	214.4	57.7
2012–02	−1276.0	38.9	−1229.3	82.7	689.6	57.0
2012–03	−1283.1	38.8	−1185.0	82.5	739.9	56.9
2012–04	−1360.1	38.9	−1129.0	82.7	695.3	57.0
2012–05	−1247.1	39.0	−1396.5	82.9	455.8	57.2
2012–06	−1398.5	39.1	−1489.8	83.1	344.1	57.3
2012–07	−1372.1	39.1	−1353.2	83.2	449.1	57.3
2012–08	−1748.4	39.1	−1569.4	83.2	600.5	57.3
2012–09	−1780.5	39.1	−1330.1	83.2	648.5	57.3
2012–10	−1785.9	39.1	−1509.4	83.1	685.0	57.3
2012–11	−1573.6	39.2	−1276.0	83.2	669.6	57.4
2012–12	−1541.3	39.5	−1070.5	83.9	804.1	57.8

(*continued on next page*)

Table A.1 (*continued*)

Date	GREENLAND		WEST ANTARCTICA		EAST ANTARCTICA	
	Ice dynamics anomaly (Gt)	Rate of ice dynamics anomaly uncertainty (Gt/yr)	Ice dynamics anomaly (Gt)	Rate of ice dynamics anomaly uncertainty (Gt/yr)	Ice dynamics anomaly (Gt)	Rate of ice dynamics anomaly uncertainty (Gt/yr)
2013–01	−1522.3	40.2	−1338.0	85.4	905.4	58.9
2013–02	−1651.6	41.2	−1290.6	87.5	709.4	60.3
2013–03	−1666.3	42.0	−1345.2	89.3	1044.9	61.5
2013–04	−1789.2	42.6	−1174.8	90.5	1095.2	62.4
2013–05	−1717.9	42.7	−1040.8	90.8	1139.4	62.6
2013–06	−1706.6	42.4	−1210.8	90.2	1063.0	62.2
2013–07	−1935.7	42.0	−1335.4	89.2	1002.7	61.5
2013–08	−1691.2	41.6	−1573.3	88.4	729.1	61.0
2013–09	−1756.6	41.6	−1543.4	88.4	773.6	60.9
2013–10	−1599.3	42.0	−1351.8	89.3	809.0	61.6
2013–11	−1644.0	43.1	−1186.4	91.6	908.9	63.1
2013–12	−1793.0	44.7	−1210.1	94.9	946.8	65.4
2014–01	−1712.5	46.7	−1308.3	99.2	941.3	68.4
2014–02	−1668.4	48.7	−1391.7	103.5	961.5	71.3
2014–03	−1844.4	50.2	−1601.3	106.7	724.3	73.5
2014–04	−1691.8	51.1	−1541.8	108.7	842.7	74.9
2014–05	−1627.2	51.2	−1381.4	108.9	867.5	75.1
2014–06	−1484.5	50.7	−1377.3	107.8	842.6	74.3
2014–07	−1697.7	49.9	−1562.2	106.1	899.2	73.1
2014–08	−1887.4	49.3	−1540.5	104.8	796.0	72.2
2014–09	−2169.9	49.3	−1757.3	104.7	806.7	72.2
2014–10	−2084.4	50.0	−1706.8	106.4	602.0	73.3
2014–11	−2392.1	51.8	−1547.4	110.0	597.8	75.8
2014–12	−2059.4	54.1	−988.7	115.1	582.0	79.3
2015–01	−2344.2	43.8	−1186.7	44.1	858.7	24.7
2015–02	−2131.0	42.4	−1443.5	42.7	974.4	23.9
2015–03	−2300.1	41.7	−1392.2	42.0	867.8	23.5
2015–04	−2205.7	41.6	−1222.7	41.9	689.0	23.5
2015–05	−2008.3	42.0	−1219.6	42.3	550.1	23.7
2015–06	−2098.4	42.5	−1346.9	42.7	737.1	23.9
2015–07	−2046.3	42.7	−1556.3	43.0	665.8	24.1
2015–08	−2260.8	42.7	−1781.2	42.9	735.5	24.0
2015–09	−2290.9	42.3	−1797.8	42.6	718.2	23.9
2015–10	−2380.7	41.7	−1957.0	42.0	722.6	23.5
2015–11	−2211.7	40.8	−1710.0	41.0	584.8	23.0
2015–12	−2300.7	39.5	−1320.3	39.7	560.8	22.3
2016–01	−2332.3	38.1	−1010.0	38.3	625.9	21.5
2016–02	−2395.0	36.9	−950.5	37.1	686.6	20.8
2016–03	−2294.5	36.2	−1256.8	36.5	952.7	20.4
2016–04	−2254.6	36.2	−1168.9	36.4	915.6	20.4
2016–05	−2110.3	36.5	−1421.0	36.7	938.1	20.6
2016–06	−2144.7	36.9	−1322.1	37.1	805.7	20.8
2016–07	−2219.4	37.1	−1601.0	37.3	771.1	20.9
2016–08	−2325.2	37.0	−1762.9	37.3	673.7	20.9
2016–09	−2371.5	36.8	−1560.5	37.1	642.7	20.8
2016–10	−2339.1	36.5	−1524.6	36.7	545.8	20.6
2016–11	−2281.5	35.9	−1324.4	36.1	618.4	20.2
2016–12	−2357.6	35.1	−1554.3	35.3	783.0	19.8
2017–01	−2569.9	34.0	−1605.7	34.2	921.4	19.2
2017–02	−2727.7	33.0	−1655.5	33.2	892.7	18.6
2017–03	−2669.6	32.6	−1496.4	32.8	849.3	18.4
2017–04	−2625.7	32.5	−1646.7	32.7	1007.7	18.3
2017–05	−2493.2	32.8	−1591.2	33.0	875.5	18.5
2017–06	−2344.4	33.0	−1723.9	33.2	864.3	18.6
2017–07	−2393.9	33.1	−1770.9	33.3	781.8	18.7
2017–08	−2582.8	33.1	−1519.3	33.3	469.4	18.7
2017–09	−2599.3	33.1	−1702.1	33.3	519.3	18.7
2017–10	−2593.2	33.2	−1510.3	33.4	449.3	18.7
2017–11	−2650.1	33.1	−1715.2	33.3	532.0	18.7
2017–12	−2299.1	32.8	−1312.8	33.0	548.8	18.5
2018–01	−2355.1	32.2	−1361.0	32.4	714.1	18.1
2018–02	−2254.7	31.6	−1419.2	31.8	742.0	17.8
2018–03	−2520.3	31.4	−1511.9	31.6	739.1	17.7
2018–04	−2477.2	31.4	−1511.4	31.6	756.3	17.7
2018–05	−2131.8	31.5	−1659.0	31.7	736.2	17.8
2018–06	−2052.3	31.6	−1543.3	31.8	708.8	17.8
2018–07	−1981.5	31.6	−1528.4	31.8	641.0	17.8

(*continued on next page*)

Table A.1 (*continued*)

Date	GREENLAND		WEST ANTARCTICA		EAST ANTARCTICA	
	Ice dynamics anomaly (Gt)	Rate of ice dynamics anomaly uncertainty (Gt/yr)	Ice dynamics anomaly (Gt)	Rate of ice dynamics anomaly uncertainty (Gt/yr)	Ice dynamics anomaly (Gt)	Rate of ice dynamics anomaly uncertainty (Gt/yr)
2018–08	−2371.8	31.6	−1753.1	31.8	681.2	17.8
2018–09	−2502.7	31.8	−1666.9	32.0	579.5	17.9
2018–10	−2582.2	32.3	−1934.2	32.5	615.9	18.2
2018–11	−2630.8	32.8	−1568.3	33.0	530.6	18.5
2018–12	−2521.6	33.1	−1425.4	33.3	707.7	18.6
2019–01	−2576.6	33.1	−1600.8	33.3	877.8	18.6
2019–02	−2533.5	32.9	−1662.2	33.2	878.2	18.6
2019–03	−2415.6	32.9	−1722.6	33.1	881.0	18.5
2019–04	−2361.6	32.9	−1638.4	33.1	783.2	18.6
2019–05	−2406.2	33.0	−1727.7	33.2	772.2	18.6
2019–06	−2454.7	32.9	−1607.6	33.1	731.4	18.5
2019–07	−2599.5	32.7	−1906.2	32.9	797.7	18.5
2019–08	−2555.2	32.8	−1798.1	33.0	706.4	18.5
2019–09	−2780.8	33.2	−1684.7	33.4	586.1	18.7
2019–10	−2776.7	34.1	−1690.9	34.3	528.9	19.2
2019–11	−2655.7	35.1	−1677.0	35.3	507.2	19.8
2019–12	−2674.7	35.9	−1908.9	36.1	691.3	20.2
2020–01	−2818.9	36.4	−1724.2	36.6	631.5	20.5
2020–02	−2898.2	36.7	−1958.7	36.9	824.6	20.7
2020–03	−2707.0	36.8	−1846.4	37.0	822.9	20.7
2020–04	−2791.3	36.9	−1666.5	37.1	705.1	20.8
2020–05	−2732.1	36.8	−1612.5	37.0	603.1	20.8
2020–06	−2714.5	36.6	−1720.3	36.8	606.0	20.6
2020–07	−2770.1	36.4	−1902.5	36.6	620.5	20.5
2020–08	−2815.6	36.4	−1937.8	36.6	504.3	20.5
2020–09	−3002.9	37.0	−2032.2	37.3	542.6	20.9
2020–10	−2995.0	38.2	−1777.1	38.4	419.3	21.5
2020–11	−3023.9	39.5	−1948.8	39.8	518.3	22.3
2020–12	−3082.2	40.7	−1752.9	41.0	500.7	23.0
2021–01	−3269.3	41.6	−1971.6	41.9	776.8	23.5
2021–02	−3342.2	42.2	−2137.3	42.5	764.9	23.8
2021–03	−3260.7	42.5	−2054.0	42.7	796.8	23.9
2021–04	−2970.4	42.6	−1940.7	42.8	781.8	24.0
2021–05	−2713.0	42.4	−2017.2	42.7	763.0	23.9
2021–06	−2616.2	42.1	−2109.7	42.4	788.4	23.7
2021–07	−2851.2	41.8	−2002.2	42.1	625.9	23.6
2021–08	−3080.5	41.9	−2053.9	42.1	436.1	23.6
2021–09	−2942.0	42.6	−2215.1	42.8	444.9	24.0
2021–10	−2897.1	43.9	−2269.1	44.1	487.8	24.7

Appendix B. Formal errors of the estimated parameters

Taking into account individual spherical harmonics with the formal errors of estimated parameters from each solution, we calculate the mean spherical harmonic (SH) standard deviation (STD) parameter for each degree and each monthly solution:

$$\text{SH STD} = \sqrt{\frac{\sum_i \delta_i^2}{n_i}} \tag{B.1}$$

where i is the number of a specific degree, δ_i is a standard deviation of spherical harmonics, i.e., formal errors derived from the covariance matrix, and $n_i = 2n + 1$ is a number of spherical harmonics with the same degree n. Among the overall common SLR-GRACE period, which covers April 2004 to October 2021, we calculate the mean values, and the minimum and maximum values, all of which are illustrated in Fig. B.1. In general, GRACE solutions have the largest errors for the lowest degrees which then decrease towards degree 10, whereas SLR solutions are characterized by the smallest errors for degrees 2 and 4 and the largest errors for degrees 9 and 10.

The mean STD SH values are lower for **SLR S** than for GRACE and GRACE Follow-On up to degree 4. Even up to degree 10, some of the **SLR S** standard deviation values are lower than the maximum STD values of the GRACE solutions due to the incompleteness and inferior quality of GRACE data during the last stage of the mission. In addition, some of the minimum standard deviation values of the **SLR S** solution up to degree 5 are lower than the mean values for GRACE and GRACE Follow-On solutions.

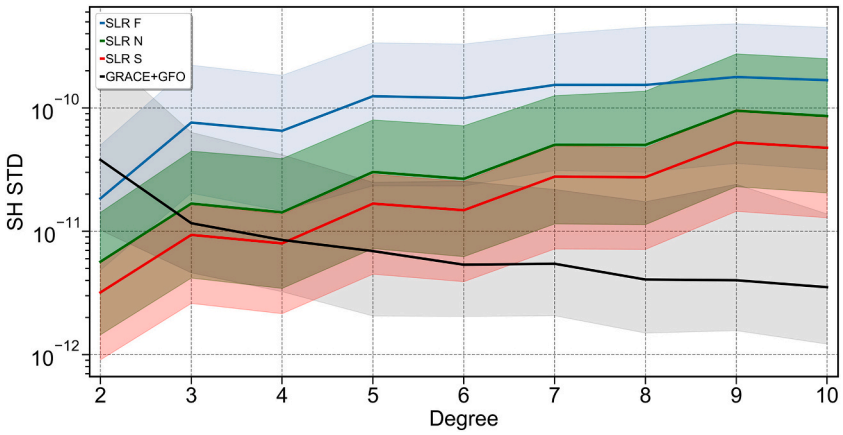

Fig. B.1. The mean standard deviation for each degree of spherical harmonics over the period from April 2004 to October 2021 – solid line. The figure also indicates the minimum and maximum values obtained for each degree as shaded areas.

Appendix C. Comparison of spherical harmonics with GRACE data

In addition to the dominating seasonal annual signals, the harmonic coefficients contain also long-term trends and other periodic signals, which are an important source of information for hydrological analysis (Cheng and Ries, 2018, 2023). Fig. B.2 shows the correlation for spherical harmonics between the time series of GRACE/GRACE-FO and SLR-based coefficients from **SLR F**, **SLR Q**, **SLR N**, and **SLR S** solutions. The correlations cover the common SLR/GRACE period from April 2004 to October 2021. The correlations between the time series of coefficients allow for the evaluation of the consistency of the signals including both the periodic signals and trends.

All the SLR-based solution show high correlation with GRACE/GRACE-Follow On for the coefficients of the degree 2 and 3. In particular, strong correlation occurs up to degree 10 and order 4. The correlations between the **SLR S** solution and the combined GRACE and GRACE Follow-On solution, which has the highest value, reach up to 0.99 for selected coefficients, e.g. S_{22} and C_{22}. Negative correlation coefficients are obtained only for a few spherical harmonic coefficients, especially those, which do not have significant gravity signals, either periodic or secular. The SLR-based sectorial spherical harmonics for which $n = m$, are typically less consistent with GRACE solutions than the spherical harmonics with low orders up to 4. However, GRACE solutions also provide sectorial harmonics of inferior quality when compared to tesseral harmonics of low degree due to the near-polar orbit and the lack of GRACE observations between satellite passes resulting in the characteristic ground track stripes. Fig. B.2 also shows that the correlation between the **SLR F** solution and the GRACE and GRACE Follow-On solutions is low for the majority of coefficients, except for degree 2, confirming the low performance of the unconstrained **SLR F** solutions due to the inversion instability.

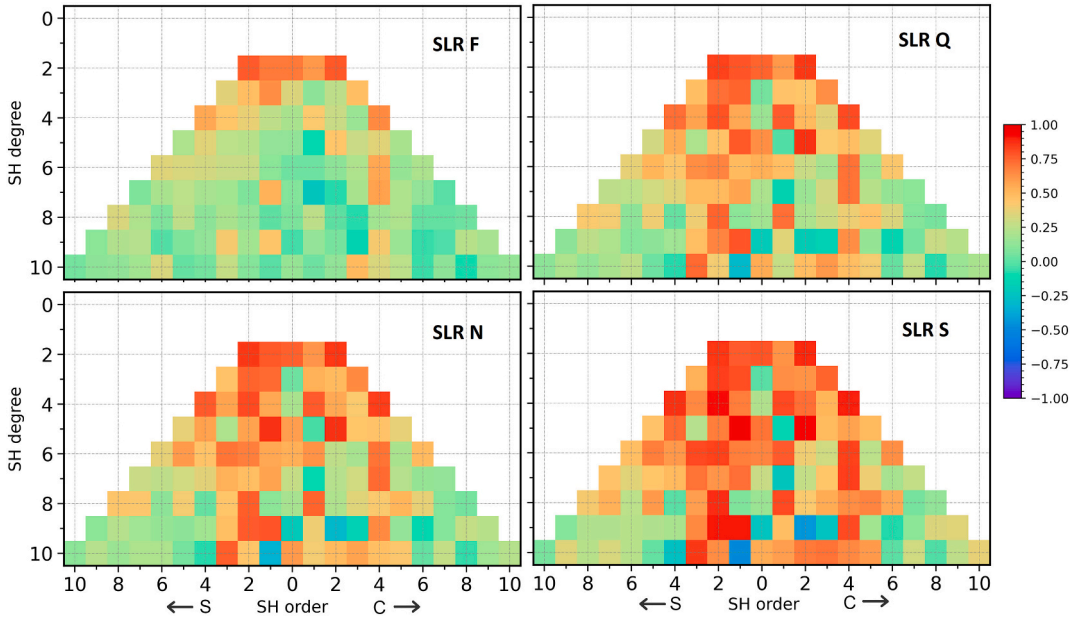

Fig. B.2. Spherical harmonics correlation between GRACE/GRACE-FO and: SLR F (upper left), SLR Q (upper right), SLR N (bottom left), SLR S (bottom right). Correlations cover the period from April 2002 to October 2021.

Fig. B.3 shows the mean correlation values calculated for the time series of individual spherical harmonics coefficients between GRACE/GRACE-FO and different SLR-based solutions and HLSST. The mean values for each degree are given to compare the even-degree and odd-degree spherical harmonics. For the **SLR N**, **SLR Q** and **SLR S** models, the values of the even-degree harmonics are more correlated than the odd-degree. For example, degree 4 is much more correlated with GRACE than degree 3, whereas degree-6 harmonics are more correlated than degree 5. Thus, the SLR solutions can derive even-degree coefficients of a better quality and more consistent with GRACE data than for the odd-degree terms. One should bear in mind

that only even-degree zonal gravity field coefficients cause secular rates of some Keplerian orbit parameters, such as the right ascension of ascending node or argument of perigee. The odd-degree terms neither cause any secular rates of the ascending node nor of perigee, thus, observations of these perturbations cannot be used for the odd-degree coefficients recovery. The odd-degree terms may only cause periodic variations in these Keplerian parameters whose amplitudes strongly depend on the orbital eccentricity (Kaula, 1966).

The average correlation for each degree from SLR solutions decreases with the increasing degree for each solution. However, for **SLR F** the mean correlation coefficients with GRACE are larger than 0.4 only for degree 2, whereas for **SLR S**, the correlations above 0.4 are for degrees between 2 and 8. Therefore, **SLR F** is strongly contaminated by a noise which prevents the recovery of the proper gravity signals. Instead, **SLR S** provides a useful gravity signal for the majority of the coefficients.

The correlations of the HLSST model with the GRACE and GRACE Follow-On solutions are also included in Fig. B.3 for comparison. The correlation coefficients between HLSST and GRACE remain at a comparable level for each of the degrees, however, strong numerical filters were applied for each coefficient in HLSST substantially reducing the solution noise.

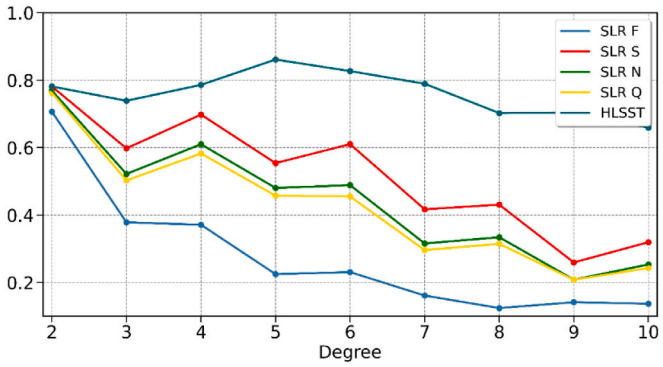

Fig. B.3. Degree-specific correlations for the value of spherical harmonics of SLR solutions and HLSST monthly solutions over the common period from April 2002 to October 2021.

References

Bianco, G., Devoti, R., Fermi, M., Luceri, V., Rutigliano, P., Sciarretta, C., 1998. Estimation of low degree geopotential coefficients using SLR data. Planet. Space Sci. 46 (11), 1633–1638. https://doi.org/10.1016/S0032-0633(97)00215-8.

Blewitt, G., 2003. Self-consistency in reference frames, geocenter definition, and surface loading of the solid Earth. J. Geophys. Res. Solid Earth 108 (B2). https://doi.org/10.1029/2002JB002082.

Bloßfeld, M., Müller, H., Gerstl, M., Štefka, V., Bouman, J., Göttl, F., Horwath, M., 2015. Second-degree stokes coefficients from multi-satellite SLR. J. Geodesy 89 (9), 857–871. https://doi.org/10.1007/s00190-015-0819-z.

Bonin, J.A., Chambers, D.P., Cheng, M., 2018. Using satellite laser ranging to measure ice mass change in Greenland and Antarctica. Cryosphere 12 (1), 71–79. https://doi.org/10.5194/tc-12-71-2018.

Caron, L., Ivins, E.R., Larour, E., Adhikari, S., Nilsson, J., Blewitt, G., 2018. GIA model statistics for GRACE hydrology, cryosphere, and ocean science. Geophys. Res. Lett. 45 (5), 2203–2212. https://doi.org/10.1002/2017GL076644.

Chen, J.L., Wilson, C.R., 2003. Low degree gravitational changes from earth rotation and geophysical models. Geophys. Res. Lett. 30 (24) https://doi.org/10.1029/2003GL018688.

Chen, J.L., Wilson, C.R., 2008. Low degree gravity changes from GRACE, Earth rotation, geophysical models, and satellite laser ranging. J. Geophys. Res. Solid Earth 113 (B6). https://doi.org/10.1029/2007JB005397.

Chen, J.L., Wilson, C.R., Seo, K.-W., 2009. S2 tide aliasing in GRACE time-variable gravity solutions. J. Geodesy 83 (7), 679–687. https://doi.org/10.1007/s00190-008-0282-1.

Chen, J., Tapley, B., Tamisiea, M.E., Save, H., Wilson, C., Bettadpur, S., Seo, K.W., 2021. Error assessment of GRACE and GRACE follow-on mass change. J. Geophys. Res. Solid Earth 126 (9), 1–18. https://doi.org/10.1029/2021JB022124.

Cheng, M., 2017. Laser Ranging in 5×5 Spherical Harmonics. https://doi.org/10.5281/zenodo.831745.

Cheng, M., Ries, J.C., 2018. Decadal variation in Earth's oblateness (J2) from satellite laser ranging data. Geophys. J. Int. 212 (2), 1218–1224. https://doi.org/10.1093/gji/ggx483.

Cheng, M., Ries, J., 2023. C20 and C30 variations from SLR for GRACE/GRACE-FO science applications. J. Geophys. Res. Solid Earth 128 (2). https://doi.org/10.1029/2022JB025459 e2022JB025459.

Cheng, M.K., Shum, C.K., Tapley, B.D., 1997. Determination of long-term changes in the Earth's gravity field from satellite laser ranging observations. J. Geophys. Res. Solid Earth 102 (B10), 22377–22390. https://doi.org/10.1029/97JB01740.

Dach, R., Lutz, S., Walser, P., Fridez, P. (Eds.), 2015. Bernese GNSS Software Version 5.2. User Manual.

Dahle, C., Arnold, D., Bezdek, A., Doornbos, E., Ellmer, M., Guo, J., Dahle, C., Zhang, Y., Jäggi, A., Klokocník, J., Krauss, S., Mao, X., Mayer-Gürr, T., Meyer, U., Sebera, J., Shum, C.K., Zhang, C., 2020. Description of the multi-approach gravity field models from swarm GPS data. Earth Syst. Sci. Data 12 (2), 1385–1417. https://doi.org/10.5194/essd-12-1385-2020.

Dobslaw, H., Bergmann-Wolf, I., Dill, R., Poropat, L., Thomas, M., Dahle, C., Esselborn, S., König, R., Flechtner, F., 2017. A new high-resolution model of non-tidal atmosphere and ocean mass variability for de-aliasing of satellite gravity observations: AOD1B RL06. Geophys. J. Int. 211 (1), 263–269. https://doi.org/10.1093/gji/ggx302.

Jacob, T., John Wahr, W., Pfeffer, T., Swenson, S., 2012. Recent contributions of glaciers and ice caps to sea level rise. Nature 482 (7386), 514–518. https://doi.org/10.1038/nature10847.

Kaula, W.M., 1966. Theory of Satellite Geodesy. Blaisdell Publishing Company, Waltham, Massachusetts.

Kvas, A., Brockmann, J.M., Krauss, S., Schubert, T., Gruber, T., Meyer, U., Mayer-Gürr, T., Schuh, W.D., Jäggi, A., Pail, R., 2021. GOCO06s – a satellite-only global gravity field model. Earth Syst. Sci. Data 13 (1), 99–118. https://doi.org/10.5194/essd-13-99-2021.

Landerer, F.W., Flechtner, F.M., Save, H., Webb, F.H., Bandikova, T., Bertiger, W.I., Bettadpur, S.V., Byun, S.H., Dahle, C., Dobslaw, H., Fahnestock, E., Harvey, N., Kang, Z., Gerhard, L., Kruizinga, H., Loomis, B.D., McCullough, C., Murböck, M., Nagel, P., Paik, M., Pie, N., Poole, S., Strekalov, D., Tamisiea, M.E., Wang, F., Watkins, M.M., Wen, H.-Y., Wiese, D.N., Yuan, D.-N., 2020. Extending the global mass change data record: GRACE follow-on instrument and science data performance. Geophys. Res. Lett. 47 (12) https://doi.org/10.1029/2020GL088306 e2020GL088306.

Löcher, A., Kusche, J., 2021. A hybrid approach for recovering high-resolution temporal gravity fields from satellite laser ranging. J. Geodesy 95 (1), 1–15. https://doi.org/10.1007/s00190-020-01460-x.

Loomis, B.D., Rachlin, K.E., Luthcke, S.B., 2019. Improved earth oblateness rate reveals increased ice sheet losses and mass-driven sea level rise. Geophys. Res. Lett. 46 (12), 6910–6917. https://doi.org/10.1029/2019GL082929.

Loomis, B., Rachlin, K.E., Wiese, D.N., Landerer, F.W., Luthcke, S.B., 2020. Replacing GRACE/GRACE-FO C30 with satellite laser ranging: impacts on Antarctic ice sheet mass change. Geophys. Res. Lett. 47 (3), 1–7. https://doi.org/10.1029/2019GL085488.

Luthcke, S.B., Sabaka, T.J., Loomis, B.D., Arendt, A.A., McCarthy, J.J., Camp, J., 2013. Antarctica, Greenland and Gulf of Alaska land-ice evolution from an iterated GRACE global mascon solution. J. Glaciol. 59 (216), 613–631. https://doi.org/10.3189/2013JoG12J147.

Maier, A., Krauss, S., Hausleitner, W., Baur, O., 2012. Contribution of satellite laser ranging to combined gravity field models. Adv. Space Res. 49 (3), 556–565. https://doi.org/10.1016/j.asr.2011.10.026.

Mao, X., Arnold, D., Girardin, V., Villiger, A., Jäggi, A., 2021. Dynamic GPS-based LEO orbit determination with 1 cm precision using the Bernese GNSS software. Adv. Space Res. 67 (2), 788–805. https://doi.org/10.1016/j.asr.2020.10.012.

Matsuo, K., Chao, B.F., Otsubo, T., Heki, K., 2013. Accelerated ice mass depletion revealed by low-degree gravity field from satellite laser ranging: Greenland, 1991-2011. Geophys. Res. Lett. 40 (17), 4662–4667. https://doi.org/10.1002/grl.50900.

Mayer-Gürr, T., Behzadpour, S., Ellmer, M., Kvas, A., Klinger, B., Strasser, S., Zehentner, N., 2018. ITSG-Grace2018 - Monthly, Daily and Static Gravity Field Solutions from GRACE. https://doi.org/10.5880/ICGEM.2018.003.

Meyer, U., Sosnica, K., Dach, R., Jäggi, A., 2019. SLR, GRACE and swarm gravity field determination and combination. Remote Sens. (Basel) 11 (8), 1–22. https://doi.org/10.3390/rs11080956.

Meyer, U., Jaeggi, A., Dahle, C., Flechtner, F., Kvas, A., Behzadpour, S., Mayer-Gürr, T., Bourgogne, S., 2020a. International combination service for time-variable gravity fields (COST-G) monthly GRACE series. GFZ Data Serv. https://doi.org/10.5880/ICGEM.COST-G.001.

Meyer, U., Lasser, M., Jaeggi, A., Dahle, C., Flechtner, F., Kvas, A., Behzadpour, S., Mayer-Gürr, T., Lemoine, J.-M., Koch, I., Flury, J., Bourgogne, S., Bourgogne, S., 2020b. International combination service for time-variable gravity fields (COST-G) monthly GRACE-FO series. GFZ Data Services. https://doi.org/10.5880/ICGEM.COST-G.002.

Otosaka, I.N., Shepherd, A., Ivins, E.R., Schlegel, N.J., Amory, C., van den Broeke, M.R., Horwath, M., Joughin, I., King, M.D., Krinner, G., Nowicki, S., Payne, A.J., Rignot, E., Scambos, T., Simon, K.M., Smith, B.E., Sørensen, L.S., Velicogna, I., Whitehouse, P.L., Agosta, G.A.C., Ahlstrøm, A.P., Blazquez, A., Colgan, W., Engdahl, M.E., Fettweis, X., Forsberg, R., Gallée, H., Gardner, A., Gilbert, L., Gourmelen, N., Groh, A., Gunter, B.C., Harig, C., Helm, V., Khan, S.A., Kittel, C., Konrad, H., Langen, P.L., Lecavalier, B.S., Liang, C.C., Loomis, B.D., McMillan, M., Melini, D., Mernild, S.H., Mottram, R., Mouginot, J., Nilsson, J., Noël, B., Pattle, M. E., Peltier, W.R., Pie, N., Roca, M., Sasgen, I., Save, H.V., Seo, K.W., Scheuchl, B., Schrama, E.J.O., Schröder, L., Simonsen, S.B., Slater, T., Spada, G., Sutterley, T.C., Vishwakarma, B.D., van Wessem, J.M., Wiese, D., van der Wal, W., Wouters, B., 2023. Mass balance of the Greenland and Antarctic ice sheets from 1992 to 2020. Earth Syst. Sci. Data 15 (4), 1597–1616. https://doi.org/10.5194/essd-15-1597-2023.

Pearlman, M., Arnold, D., Davis, M., Barlier, F., Biancale, R., Vasiliev, V., Ciufolini, I., Paolozzi, A., Pavlis, E.C., Sośnica, K., Bloßfeld, M., 2019a. Laser geodetic satellites: A high-accuracy scientific tool. J. Geodesy 93 (11), 2181–2194. https://doi.org/10.1007/s00190-019-01228-y.

Pearlman, M.R., Noll, C.E., Pavlis, E.C., Lemoine, F.G., Combrink, L., Degnan, J.J., Kirchner, G., Schreiber, U., 2019b. The ILRS: approaching 20 years and planning for the future. J. Geodesy 93 (11), 2161–2180. https://doi.org/10.1007/s00190-019-01241-1.

IERS conventions 2010 (IERS Technical Note 36). In: Petit, G., Luzum, B. (Eds.), 2010. Verlag des Bundesamts für Kartographie und Geodäsie. Retrieved from. http://iers-conventions.obspm.fr.

Richter, H., Maja, P., Lück, C., Klos, A., Sideris, M.G., Rangelova, E., Kusche, J., 2021. Reconstructing GRACE-type time-variable gravity from the swarm satellites. Sci. Rep. 11 (1), 1117. https://doi.org/10.1038/s41598-020-80752-w.

Rodell, M., Famiglietti, J.S., Wiese, D.N., Reager, J.T., Beaudoing, H.K., Landerer, F.W., Lo, M.H., 2018. Emerging trends in global freshwater availability. Nature 557 (7707), 651–659. https://doi.org/10.1038/s41586-018-0123-1.

Shepherd, A., Ivins, E.R., Geruo, A., Barletta, V.R., Bentley, M.J., Bettadpur, S., Briggs, K. H., Bromwich, D.H., Forsberg, R., Galin, N., Horwath, M., Jacobs, S., Joughin, I., King, M.A., Lenaerts, J.T.M., Li, J., Ligtenberg, S.R.M., Luckman, A., Luthcke, S.B., McMillan, M., Meister, R., Milne, G., Mouginot, J., Muir, A., Nicolas, J.P., Paden, J., Payne, A.J., Pritchard, H., Rignot, E., Rott, H., Sørensen, L.S., Scambos, T.A., Scheuchl, B., Schrama, E.J.O., Smith, B., Sundal, A.V., van Angelen, J.H., van de Berg, W.J., van den Broeke, M.R., Vaughan, D.G., Velicogna, I., Wahr, J., Whitehouse, P.L., Wingham, D.J., Yi, D., Young, D., Jay Zwally, H., 2012. A reconciled estimate of ice-sheet mass balance. Science 338 (6111), 1183–1189. https://doi.org/10.1126/science.1228102.

Shepherd, A., Ivins, E., Rignot, E., Smith, B., van den Broeke, M., Velicogna, I., Whitehouse, P., Briggs, K., Joughin, I., Krinner, G., Nowicki, S., Payne, T., Scambos, T., Schlegel, N., Geruo, A., Agosta, C., Ahlstrøm, A., Babonis, G., Barletta, V., Blazquez, A., Bonin, J., Csatho, B., Cullather, R., Felikson, D., Fettweis, X., Forsberg, R., Gallee, H., Gardner, A., Gilbert, L., Groh, A., Gunter, B., Hanna, E., Harig, C., Helm, V., Horvath, A., Horwath, M., Khan, S., Kjeldsen, K.K., Konrad, H., Langen, P., Lecavalier, B., Loomis, B., Luthcke, S., McMillan, M., Melini, D., Mernild, S., Mohajerani, Y., Moore, P., Mouginot, J., Moyano, G., Muir, A., Nagler, T., Nield, G., Nilsson, J., Noel, B., Otosaka, I., Pattle, M.E., Peltier, W.R., Pie, N., Rietbroek, R., Rott, H., Sandberg-Sørensen, L., Sasgen, I., Save, H., Scheuchl, B., Schrama, E., Schröder, L., Seo, K.-W., Simonsen, S., Slater, T., Spada, G., Sutterley, T., Talpe, M., Tarasov, L., van de Berg, W.J., van der Wal, W., van Wessem, M., Vishwakarma, B.D., Wiese, D., Wouters, B., The IMBIE Team, 2018. Mass balance of the Antarctic ice sheet from 1992 to 2017. Nature 558 (7709), 219–222. https://doi.org/10.1038/s41586-018-0179-y.

Shepherd, A., Ivins, E., Rignot, E., Smith, B., van den Broeke, M., Velicogna, I., Whitehouse, P., Briggs, K., Joughin, I., Krinner, G., Nowicki, S., Payne, T., Scambos, T., Schlegel, N., Geruo, A., Agosta, C., Ahlstrøm, A., Babonis, G., Barletta, V.R., Bjørk, A.A., Blazquez, A., Bonin, J., Colgan, W., Csatho, B., Cullather, R., Engdahl, M.E., Felikson, D., Fettweis, X., Forsberg, R., Hogg, A.E., Gallee, H., Gardner, A., Gilbert, L., Gourmelen, N., Groh, A., Gunter, B., Hanna, E., Harig, C., Helm, V., Horvath, A., Horwath, M., Khan, S., Kjeldsen, K.K., Konrad, H., Langen, P.L., Lecavalier, B., Loomis, B., Luthcke, S., McMillan, M., Melini, D., Mernild, S., Mohajerani, Y., Moore, P., Mottram, R., Mouginot, J., Moyano, G., Muir, A., Nagler, T., Nield, G., Nilsson, J., Noël, B., Otosaka, I., Pattle, M.E., Richard Peltier, W., Pie, N., Rietbroek, R., Rott, H., Sørensen, L.S., Sasgen, I., Save, H., Scheuchl, B., Schrama, E., Schröder, L., Seo, K.-W., Simonsen, S.B., Slater, T., Spada, G., Sutterley, T., Talpe, M., Tarasov, L., van de Berg, W.J., van der Wal, W., van Wessem, M., Vishwakarma, B.D., Wiese, D., Wilton, D., Wagner, T., Wouters, B., Wuite, J., The IMBIE Team, 2020. Mass balance of the Greenland ice sheet from 1992 to 2018. Nature 579 (7798), 233–239. https://doi.org/10.1038/s41586-019-1855-2.

Sośnica, K., Jäggi, A., Meyer, U., Thaller, D., Beutler, G., Arnold, D., Dach, R., 2015. Time variable Earth's gravity field from SLR satellites. J. Geodesy 89 (10), 945–960. https://doi.org/10.1007/s00190-015-0825-1.

Sun, Y., Li, Y., Guo, X., Guo, J., 2023. Estimating C30 coefficients for GRACE/GRACE-FO time-variable gravity field models using the GRACE-OBP approach. J. Geodesy 97 (3), 20. https://doi.org/10.1007/s00190-023-01707-3.

Syed, T.H., Famiglietti, J.S., Chambers, D.P., Willis, J.K., Hilburn, K., 2010. Satellite-based global-ocean mass balance estimates of interannual variability and emerging trends in continental freshwater discharge. Proc. Natl. Acad. Sci. 107 (42), 17916–17921. https://doi.org/10.1073/pnas.1003292107.

Tapley, B.D., Bettadpur, S., Ries, J.C., Thompson, P.F., Watkins, M.M., 2004. GRACE measurements of mass variability in the Earth system. Science 305 (5683), 503–505. https://doi.org/10.1126/science.1099192.

Tepes, P., Gourmelen, N., Nienow, P., Tsamados, M., Shepherd, A., Weissgerber, F., 2021. Changes in elevation and mass of Arctic glaciers and ice caps, 2010–2017. Remote Sens. Environ. 261, 112481 https://doi.org/10.1016/j.rse.2021.112481.

Velicogna, I., Wahr, J., 2013. Time-variable gravity observations of ice sheet mass balance: precision and limitations of the GRACE satellite data. Geophys. Res. Lett. 40 (12), 3055–3063. https://doi.org/10.1002/grl.50527.

Velicogna, I., Sutterley, T.C., van den Broeke, M.R., 2014. Regional acceleration in ice mass loss from Greenland and Antarctica using GRACE time-variable gravity data. Geophys. Res. Lett. 41 (22), 8130–8137. https://doi.org/10.1002/2014GL061052.

Wake, L.M., Lecavalier, B.S., Bevis, M., 2016. Glacial isostatic adjustment (GIA) in Greenland: a review. Curr. Climate Change Rep. 2 (3), 101–111. https://doi.org/10.1007/s40641-016-0040-z.

Wang, Z., Zhang, B., Yao, Y., Zhang, W., 2023. GRACE and mass budget method reveal decelerated ice loss in East Greenland in the past decade. Remote Sens. Environ. 286, 113450 https://doi.org/10.1016/j.rse.2023.113450.

Weigelt, M., 2019. Time Series of Monthly Combined HLSST and SLR Gravity Field Models to Bridge the Gap between GRACE and GRACE-FO: QuantumFrontiers_HLSST_SLR_COMB2019s. GFZ Data Services.

Wu, X., Heflin, M.B., Ivins, E.R., Fukumori, I., 2006. Seasonal and interannual global surface mass variations from multisatellite geodetic data. J. Geophys. Res. Solid Earth 111 (B9). https://doi.org/10.1029/2005JB004100.

Zajdel, R., Sośnica, K., Drożdżewski, M., Bury, G., Strugarek, D., 2019. Impact of network constraining on the terrestrial reference frame realization based on SLR observations to LAGEOS. J. Geod. 93 (11), 2293–2313. https://doi.org/10.1007/s00190-019-01307-0.